University of Thessaly
School of Engineering
Department of Mechanical Engineering

Three–Dimensional Flow Analysis in the Calendering Process

A Thesis
Submitted in partial fulfillment of the requirements for the degree of
Master of Science (M.Sc.)
Of the Department of Mechanical Engineering of University of Thessaly

by

Nickolaos D. Polychronopoulos
B.Sc. in Materials Science

Advisory Committee:
Assoc. Prof. T.D. Papathanasiou, supervisor
Prof. N. Pelekasis
Prof. P. Tsiakaras

Volos 2012

Η έγκριση της μεταπτυχιακής εργασίας από το Τμήμα Μηχανολόγων Μηχανικών της Πολυτεχνικής Σχολής του Πανεπιστημίου Θεσσαλίας δεν υποδηλώνει αποδοχή των απόψεων του συγγραφέα (Ν. 5343/32 αρ. 202 παρ. 2).

Τὰ πάντα ῥεῖ, τὰ πάντα χωρεῖ καὶ οὐδὲν μένει.

Ηράκλειτος, 554 π.Χ. – 484 π.Χ.

Acknowledgements

I am most grateful to my supervisor Assoc. Prof. Thanasis D. Papathanasiou for his guidance, criticism and continuous support during my Master's Degree. I would like to thank Prof. Nikolaos Pelekasis, for his valuable knowledge in Fluid Mechanics and computational algorithms for fluid flows. I would also like to thank Prof. Panagiotis Tsiakaras and Assoc. Prof. Nikolaos Andritsos for their crucial contribution in understanding the true meaning of physical phenomena. I would like to thank Prof. Emeritus of McMaster University, John Vlachopoulos, for his guidance and continuous effort to conceive in the best possible way on how nature works and getting me one step further, beyond the mathematical equations. Very special thanks go to Dr. Ioannis Sarris, Dr. Sotirios Kakarantzas and Dr. Christos Dritselis for their help in understanding the meaning of Computational Fluid Dynamics. I would like also to thank my family for their true support and my friends, Petros Christodoulou and Dimitris Tsokolis for their memorable company and friendship. Last but not least, I would like to thank, the PhD candidate and my friend, Lefteris Benos, for the inexhaustible conversations to understand the strange paths of nature.

Objectives

The importance to study the calendering process lies to the fact of the high volume capacities and that the formed sheet can have very high quality. Thus, operating variables used in engineering calculations need to be evaluated beforehand with the most important being the maximum pressure that develops in the process. Pressure distribution is developed in the machine and cross–machine direction, primarily due to the rotational movement of the calenders. A lot of work has been carried out in the past on an effort to study the flow numerically using one–dimensional or two–dimensional models as well as experimentally. However, there are very few studies concerning the three–dimensional effects occurring during the physical process. These effects, which in the past were observed experimentally, are the pressure distribution in the cross–machine direction which is described by a quasi–parabolic pressure profile, the spiraling flow pattern of the material in the melt bank and the spreading of the sheet as it passes through the calenders. The scope and the contribution of the present work is to employ the Generalized Newtonian Fluid model and solve the fully 3D Navier–Stokes equations so that to predict the three–dimensional effects as stated above. This was carried out by making several assumptions and approximations concerning the rheological behavior of the material as well as the computational flow domain. All the numerical experiments were carried out using the *Open Source Field Operation and Manipulation* (OpenFOAM) software.

THESIS OUTLINE

In Chapter 1 a brief overview concerning the calendering process is presented, explaining the way polymeric melts form thin sheets by the process. Chapter 2 presents the mathematical formulation used to describe the process by means of the *Lubrication Approximation Theory* (LAT) and how the equations under the LAT can be derived from the well-known Navier–Stokes equations making assumptions concerning the physical behavior of polymer melts. Under certain flow conditions and geometries the Navier–Stokes can be simplified. The formulation is done for Newtonian and non–Newtonian fluids. Chapter 3 presents a literature survey concerning previous studies on the process, with the pressure distribution in the machine direction and the pattern of the flow being the most important aspects studied. The survey covers one-dimensional and two-dimensional analyses of the calendering process. In Chapter 4, the Finite Volume Method that *OpenFOAM* employs, is briefly discussed. It is presented the type of equations the software solves and how these equations were solved for the study of the calendering. In Chapter 5, the analytical solution obtained from the *Lubrication Approximation Theory* is compared against the numerical solution of the Navier–Stokes equations, using the open source software *OpenFOAM*. We consider both, Newtonian and Generalized–Newtonian Fluids utilizing the power–law and Carreau viscosity models. The dimensions of the calendering apparatus as well as the rheological parameters of the fluids were obtained from the literature and represent actual industrial equipment and real materials. The polymeric material was Poly–VinylChloride (PVC). Finally, in Chapter 6, we focus on the three-dimensional flow features of the process. There is only a limited amount of published work concerning 3D calendering and this is presented and discussed here, in light of our own 3D computational results for Newtonian and non–Newtonian fluids.

Table of Contents

Chapter 1

Introduction

The term “calender” is derived from the Greek word *Κύλινδρος* (cylinder) and according to Merriam–Webster’s International Dictionary, it means “to press (as cloth, rubber or paper) between rollers or plates in order to smooth and glaze or to thin into sheets”. Calendering is the process in which molten material is dragged through the narrow region between two rotating (counter rotating or co–rotating) heated rolls in such a way as to produce a film or sheet. Figure 1 shows a schematic representation of the calendering process. It is observed that due to the reduced area, a melt bank is created before the region where the distance between the rollers is the smallest (the nip region). In this melt bank, a very interesting flow pattern develops with multiple recirculation regions (this is shown later on the thesis). The number of rolls of a calendering line is determined primarily by the nature of the material processed as well as the desired product. For example, rubber can be processed and calendered on a two–roll calendar, with four roll calenders generally used for double coating of substrates (Figure 1.2.a). However, the surface requirements for good to excellent quality of calendered thermoplastic polymer require four–roll calenders as shown at Figures 1.2.b and 1.2.c which are the standard calender configurations typically called “inverted L” or “Z” configurations. Calender sizes range up to 900 *mm* in diameter and 2500 *mm* wide, with polymer throughputs up to 4000 *kg/h*. The surface temperature of the rollers is carefully controlled by using drilled rolls (i.e. axially drilled holes all around the periphery) in which a temperature – controlling liquid is circulated [1,2,3].

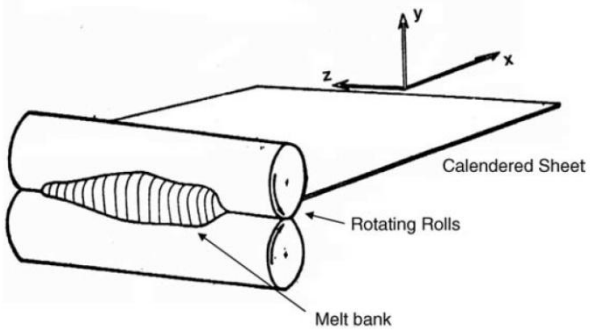

Figure 1.1. Sketch showing the calendering process between two counter–rotating rolls [3].

In an analysis of the calendering process one seeks the relationships among performance variables, such as the sheet thickness as well as design and operational variables, such as roll diameter and the speed of the rollers. Also, the effect of the different rheological parameters on these relationships is sought. Calenders may also be used for the production of a certain "finish" on a surface, either a degree of "gloss" or smoothness which might be required for a desired use, or even produce a sheet with intentional degree of roughness or pattern. Finish is a result of interaction between the fluid and the surface of the rollers in the region where the calendered sheet separates from the rollers [1].

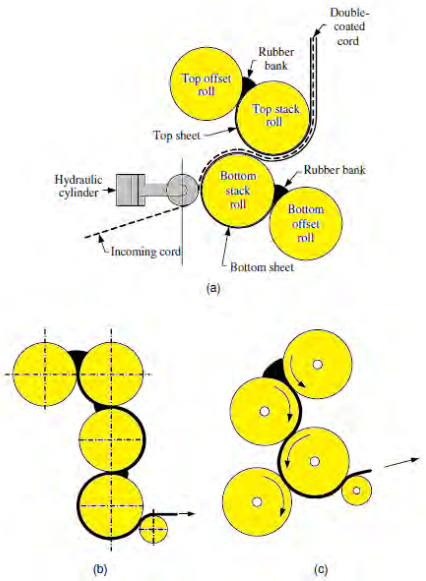

Figure 1.2. (a) A four–roll, inclined "Z" calender for double casting of tire cord. (b) A four–roll, inverted "L" calender. (c) A four – roll "Z" calender [2].

The calendering process, is commonly used for shaping high melt viscosity thermoplastic sheets and is particularly suitable for polymers susceptible to thermal degradation or containing substantial amounts of solid additives. This is due to the fact that the calender can convey large rates of melt with a small mechanical energy input (in comparison to a single–screw extruder for example).

A very important aspect in the calendering process is the thickness uniformity of the produced sheet in both the machine and cross – machine direction. Variations in gap size due to the dimensions of the roll, thermal effects, and roll distortions due to high pressures developing in the gap, will result in product nonuniformity in the cross–machine direction. Eccentricity of the roll with respect to the roll shaft, as well as roll vibration and feed uniformity, must be tightly controlled to avoid non - uniformity in the machine direction. A uniform empty gap size will be distorted in operation because of hydrodynamic forces, developed in the nip region, which deflect the rolls. From such a condition, the resulting product will be thick in the middle and thin at the edges.

Calendering lines are very expensive in terms of capital investment in machinery. Film and sheet extrusion are competitive processes because the capital investment for the extruder itself is only a fraction of the cost of a calender. However, the high quality and volume capabilities of calendering lines make them advantageous for many types of products, especially for temperature sensitive materials. Polyvinylchloride (PVC) is the major polymer that is calendered.

Chapter 2

Mathematical Formulation of Calendering

2.1 General Considerations

Polymer melts flow at very low Reynolds numbers (e.g. $Re = 10^{-2}$–10^{-4}) and the creeping flow approximation is applicable, in which, the intertial forces are very small compared to the viscous forces and the flow is steady in time. Thus, the conservation equations can be simplified into the following

$$\nabla \cdot (\rho \mathbf{U}) = 0 \tag{2.1}$$

$$0 = -\nabla p + \nabla \cdot \bar{\bar{\tau}} \tag{2.2}$$

$$\rho C_p \mathbf{U} \cdot \nabla T = \nabla \cdot (k \nabla T) + \rho \nabla \cdot \mathbf{U} + \bar{\bar{\tau}} : \nabla \mathbf{U} \tag{2.3}$$

where ρ is the density, $\mathbf{U} = \mathbf{U}(u_x,u_y,u_z)$ the velocity vector, p the pressure, $\bar{\bar{\tau}}$ the stress tensor, C_p specific heat, T temperature and k thermal conductivity. The last commonly used set of approximations in liquid flow (isothermal, as well as nonisothermal) and in conductive heat transfer, is to treat k, C_p, and ρ as constant quantities, independent of T and p. In polymer processing, where both heat transfer and flow take place, typical pressure variations may reach up to 40 *MPa* for most extrusion processes, such as flat die extrusion and this suggests density and viscosity changes. While the effect of pressure in melt density is small (perhaps 5% under the most severe extrusion conditions) the effect on viscosity is larger. Cogswell [4] suggests as a very rough approximation that 10 *MPa* of pressure have as much effect as a reduction of 5^{o}C of temperature. While, the viscosity

dependence on temperature is nearly always taken into consideration the author is not aware of any serious attempts to consider pressure dependence of viscosity in the extrusion and the calendering process. For those reasons, in the presentation below the incompressibility assumption will be used and the viscosity will be a function of shear rate but not of pressure. In the *Generalized Newtonian Fluid* (GNF) model, which will be presented later on the present study, the viscosity is always a function of temperature, usually through an exponential equation. However, in the present study any thermal effects of the process were neglected, and it was decided that the viscosity will be only a function of the shear rate. Thus, Eq. 2.1, 2.2 and 2.3 can be written in the following form

$$\nabla \cdot \mathbf{U} = 0 \tag{2.4}$$

$$0 = -\nabla p + \nabla \cdot \overline{\overline{\tau}} \tag{2.5}$$

$$\rho C_p \mathbf{U} \cdot \nabla T = k\nabla^2 T + \overline{\overline{\tau}} : \nabla \mathbf{U} \tag{2.6}$$

Moreover, assuming that the fluid does not spread as it enters the gap between the rolls, we may write Eq. 2.4, 2.5 and 2.6 in two dimensions, where *x* is the direction of the flow and *y* perpendicular to roll axis (thus neglecting phenomena in the direction of the cylinder axis), as

$$\frac{\partial u_x}{\partial x} + \frac{\partial u_y}{\partial y} = 0 \tag{2.7}$$

$$0 = -\frac{\partial p}{\partial x} + \frac{\partial \tau_{xx}}{\partial x} + \frac{\partial \tau_{xy}}{\partial y} \tag{2.8}$$

$$0 = -\frac{\partial p}{\partial y} + \frac{\partial \tau_{yx}}{\partial x} + \frac{\partial \tau_{yy}}{\partial y} \tag{2.9}$$

$$\rho C_p \left(u_x \frac{\partial T}{\partial x} + u_y \frac{\partial T}{\partial y} \right) = k \left(\frac{\partial^2 T}{\partial x^2} + \frac{\partial^2 T}{\partial y^2} \right) + \tau_{xx} \frac{\partial u_x}{\partial x} + \tau_{xy} \frac{\partial u_x}{\partial y} + \tau_{yx} \frac{\partial u_y}{\partial x} + \tau_{yy} \frac{\partial u_y}{\partial y} \tag{2.10}$$

Furthermore, it can be assumed that the most important effect in the calendering process, namely the build-up of pressure and the orientation of the polymeric molecules, occur in the region of the minimal roll separation, which is called *nip region*.

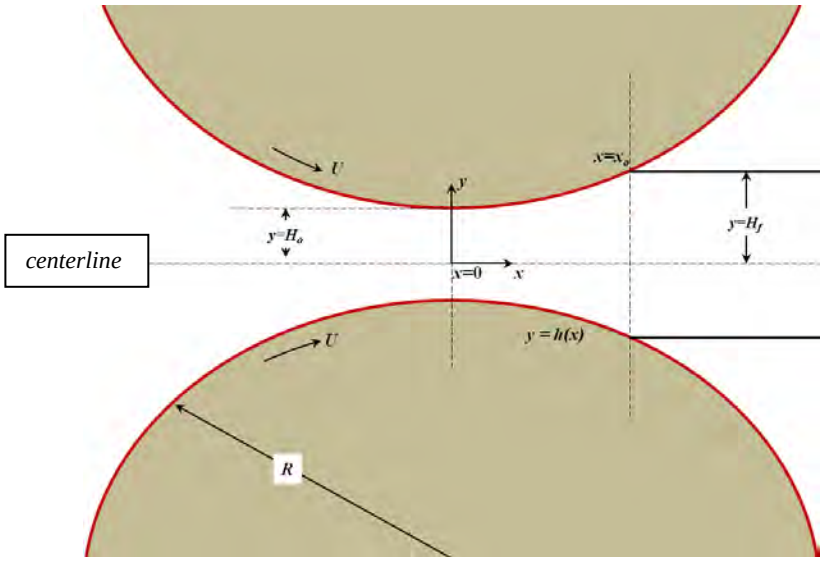

Figure 2.1. Schematic representation for definition of the calendering flow analysis with the Lubrication Approximation Theory.

In that region and extending to either side (in the ±x direction) by a distance of the order of x_f as shown in Figure 2.1, the roll surfaces are nearly parallel if, as is usually the case $H_o << R$. For that reason, it is reasonable to assume that the flow in the gap will be nearly parallel so that the key assumptions of the *Lubrication Approximation Theory* (LAT) may be applied

$$\frac{\partial}{\partial x} << \frac{\partial}{\partial y}, \quad u_y << u_x, \quad u_x = u_x(x,y) \quad \text{and} \quad p = p(x)$$

thus we have

$$\frac{\partial u_x}{\partial x} + \frac{\partial u_y}{\partial y} = 0 \tag{2.11}$$

$$0 = -\frac{dp}{dx} + \frac{\partial \tau_{xy}}{\partial y} \tag{2.12}$$

$$\rho C_p u_x \frac{\partial T}{\partial x} = k \frac{\partial^2 T}{\partial y^2} + \tau_{xy} \frac{\partial u_x}{\partial y} \tag{2.13}$$

The process of transforming problems from Eq. 2.8 and 2.9 into Eq. 2.12 is often referred to as *Lubrication Approximation.* The reference to *lubrication* comes from the fact that lubrication problems themselves typically involve a geometry such that Eq. 2.12 is valid. The continuity equation (Eq. 2.11) may be replaced by the integral form

$$Q = 2 \int_0^{h(x)} u_x dy \tag{2.14}$$

where Q is the volumetric flow rate.

For the above equations to be solved a constitutive equation that relates stress to the rate of strain is also needed. Constitutive equations are relations between stresses and strains (deformations) and are solved together along with the continuity and momentum equations. In its simplest form (simple shear flow), the Newtonian equation is a linear relation between the shear stress and the shear rate

$$\tau = \eta \dot{\gamma} = \eta \frac{du_x}{dy} \tag{2.15}$$

where $\dot{\gamma}$ is the shear rate. This expression for $\dot{\gamma}$ is valid for simple shear flows between two flat plates for instance, and it is directly applicable to unidirectional flows. In polymer processing, however, most interesting flow problems require two– or three–dimensional analyses (like the present study), of creeping (low Reynolds, *Re*<<1) flows and the shear rate is expressed in a tensor form that will be subsequently presented.

The stress tensor $\overline{\overline{\tau}}$, in Eq. 2.5 is a (second order) tensor as shown below

$$\overline{\overline{\tau}} \Rightarrow \begin{pmatrix} \tau_{xx} & \tau_{xy} & \tau_{xz} \\ \tau_{yx} & \tau_{yy} & \tau_{yz} \\ \tau_{zx} & \tau_{zy} & \tau_{zz} \end{pmatrix} \tag{2.16}$$

To generalize the Newtonian equation in three dimensions we must propose a linear relation between stress components and rate of strain components. The rate of strain tensor is the following

$$\overline{\overline{D}} = \frac{1}{2}\left(\nabla \mathbf{u} + \nabla \mathbf{u}^T\right) = \frac{1}{2}\left(\frac{\partial u_i}{\partial x_j} + \frac{\partial u_j}{\partial x_i}\right) \tag{2.17}$$

Where the components of the velocity gradient tensor, $\nabla \mathbf{u}$ are the following

$$\nabla u_{i,j} = \frac{\partial u_i}{\partial x_j} \tag{2.18}$$

and

$$\overline{\overline{D}} \Rightarrow \begin{pmatrix} D_{xx} & D_{xy} & D_{xz} \\ D_{yx} & D_{yy} & D_{yz} \\ D_{zx} & D_{zy} & D_{zz} \end{pmatrix} \tag{2.19}$$

where

$$D_{xx} = \frac{1}{2}\left(\frac{\partial u_x}{\partial x} + \frac{\partial u_x}{\partial x}\right),\ D_{xy} = \frac{1}{2}\left(\frac{\partial u_x}{\partial y} + \frac{\partial u_y}{\partial x}\right) \tag{2.20}$$

and similarly the other components can be written out explicitly in terms of the components in the *x*, *y* and *z* directions. The Newtonian constitutive equation can be generalized in the form

$$\overline{\overline{\tau}} = \eta\left(2\overline{\overline{D}}\right) \tag{2.21}$$

and this means that

$$\tau_{xx} = \eta\left(2D_{xx}\right) = 2\eta\frac{\partial u_x}{\partial x},\ \tau_{xy} = \eta\left(2D_{xy}\right) = \eta\left(\frac{\partial u_x}{\partial y} + \frac{\partial u_y}{\partial x}\right) \text{ etc.} \tag{2.22}$$

where in the above equations η is the fluid viscosity, which, under the assumption of a Newtonian fluid is constant, independent on both, shear rate and temperature. To account for the shear–thinning behavior of polymer melts, a number of models have been proposed in the literature. These include the power–law, Carreau–Yasuda (the model will be presented further on the present study) and Cross models, are generalized by replacing $\dot{\gamma}$ by the function (II_D) which is the second invariant of the strain rate tensor $2\overline{\overline{D}}$. Thus we have the power–law equation which can be written as

$$\eta = m(T)\cdot\left|\dot{\gamma}\right|^{n-1} \tag{2.23}$$

where η is the viscosity, *m* is the *consistency index* (the larger the *m* the more viscous the polymer melt), *n* is the power–law index, expressing the strength of the influence of shear rate on viscosity (for *n*=1 we have Newtonian behavior) and $\left|\dot{\gamma}\right|$ is the magnitude of the rate of strain tensor and is given by the following equation

$$\left|\dot{\gamma}\right| = \sqrt{\frac{1}{2}II_D} \tag{2.24}$$

A severe limitation of the power-law model and the source of large errors when used in 2D or 3D flows is that at very low shear rates, it predicts abnormally large viscosities and thus flow fields which can be severely unrealistic.

Other viscosity models which are widely used and do not share the above limitation, are the Carreau – Yasuda and Cross models. The Carreau – Yasuda model is the following

$$\eta(\dot{\gamma}) = \eta_o \left[1 + (\lambda\dot{\gamma})^{\frac{n-1}{a}} \right]^a \tag{2.25}$$

For α=2 the model is simply called Carreau. The Cross model is the following

$$\eta(\dot{\gamma}) = \frac{\eta_o}{1 + (\lambda\dot{\gamma})^{1-n}} \tag{2.26}$$

where η_0 is the zero–shear rate viscosity. The parameter λ is a constant with units of time. In the Carreau–Yasuda model, λ determines the shear rate at which a transition occurs from the zero–shear rate plateau to the shear thinning portion of the viscosity versus shear rate curve. In the present study, except the Newtonian model, power–law and Carreau viscosity models will be used.

In the power–law model the consistency index *m* (i.e. the value of the viscosity at shear rate $\dot{\gamma} = 1s^{-1}$) is a function of temperature in the same way as zero–shear viscosity. The power–law *n* parameter is usually not a function of temperature. The viscosity dependence of temperature is usually expressed either by an Arrhenius expression, mostly used in polymer physics and rheology

$$\eta = \eta_{ref.} \left[\frac{E}{R} \left(\frac{1}{T} - \frac{1}{T_{ref.}} \right) \right] \tag{2.27}$$

or simple exponential, mostly used in equipment design

$$\eta = \eta_{ref} \exp[-b(T - T_{ref.})] \tag{2.28}$$

where $\eta_{ref.}$ is a viscosity measured at a reference temperature, E is the activation energy and R is the gas constant. The temperature sensitivity coefficient b is usually between 0.01 and 0.1 $^{o}C^{-1}$ for most commercial polymers. For HDPE (linear polymer) the value of b is roughly 0.01, while for LDPE (branched) it may reach 0.03.

2.2 Lubrication Approximation with the Newtonian Model

For a Newtonian fluid the stress is related to the rate of strain in the following way

$$\tau_{xy} = \mu \frac{\partial u_x}{\partial y} \tag{2.29}$$

where μ is the Newtonian viscosity. The momentum equation with the Lubrication Approximation analysis for the rectangular coordinate system shown at Figure 2.1 is

$$\frac{\partial p}{\partial x} = \mu \frac{\partial^2 u_x}{\partial y^2} \tag{2.30}$$

The above equation can be solved with the no–slip and symmetry boundary conditions

$$u_x = U \text{ on } y = h(x) \quad \text{and} \quad \frac{\partial u_x}{\partial y} = 0 \text{ on } y = 0 \tag{2.31}$$

where U is the velocity of the calenders, and they give

$$u_x = U + \frac{y^2 - h^2(x)}{2\mu}\frac{dp}{dx} \tag{2.32}$$

Examining *h(x)*, which is the *y* distance from the centerline, it is easy to verify the change of that distance with respect to the position *x* along the centerline by the following expression

$$h(x) = H_o + R - \left(R^2 - x^2\right)^{1/2} \tag{2.33}$$

However, in order to simplify the analysis the above equation can be expressed with a remarkable degree of accuracy by a second order polynomial since it is more likely to confine the analysis to values that $x<<R$. Thus Eq. 2.33 can be approximated as

$$h(x) = H_o\left(1 + \frac{x^2}{2H_oR}\right) \tag{2.34}$$

The above equation actually treats the surfaces of the calenders as parabolic. It is convenient now to define a set of dimensionless variables as below

$$x' = \frac{x}{\sqrt{2RH_o}} \qquad y' = \frac{y}{H_o}$$

$$u_x' = \frac{u_x}{U} \qquad p' = \frac{pH_o}{\mu U}$$

Then, we can find an expression for the pressure gradient from the integrated form of the continuity equation (Eq. 2.14) like below

$$Q = 2\int_0^{h(x)} u_x dy = 2h(x)\left[U - \frac{h^2(x)}{3\mu}\frac{dp}{dx}\right] \tag{2.35}$$

Then the equation above can be solved for *dp/dx* and find in dimensionless form

$$\frac{dp'}{dx'} = \sqrt{\frac{18R}{H_o}} \frac{x'^2 - \lambda^2}{\left(1 + x'^2\right)^3} \tag{2.36}$$

where λ is a dimensionless parameter

$$\lambda^2 = \frac{H(x)}{H_o} - 1 \tag{2.37}$$

From a physical point of view, the effects occurring at the detachment point (i.e. at $y=H_f$ and $x=x_f$), will exert a strong influence on the overall behavior of the process. Eq. 2.36 gives zero pressure gradient at $x' = \pm\lambda$. The distance $x' = \lambda$ represents the point where the sheet leaves the rolls (the point of detachment) and $x' = -\lambda$ is the point of maximum pressure. The point of detachment is obtained if we ignore the forces acting at the separation boundary and then we expect the stress just inside the fluid to be the same as the ambient pressure. It is also assumed that right at separation, the profile is flat and the viscous stresses vanish at that point. The flat profile corresponds to $\partial u_x / \partial y = 0$ and $\partial^2 u_x / \partial y^2 = 0$. For those reasons the boundary condition for the pressure at the detachment point is the following

$$p' = 0 \quad \text{at} \quad x' = \lambda \tag{2.38}$$

Eq. 2.36 may be integrated with respect to x' and if the boundary condition of Eq. 2.38 is imposed, then the solution for $p'(x')$ is found to be the following

$$p' = \sqrt{\frac{9R}{32H_o}} \left[\frac{x'^2\left(1 - 3\lambda^2\right) - 1 - 5\lambda^2}{\left(1 + x'^2\right)^2} x' + \left(1 - 3\lambda^2\right)\left(\tan^{-1} x' - \tan^{-1} \lambda\right) + \frac{1 + 3\lambda^2}{1 + \lambda^2} \lambda \right] \tag{2.39}$$

Figure 2.2, shows qualitatively the shape of the pressure distribution along the centerline. The maximum pressure occurs just upstream, at distance $x'=-\lambda$ from the nip region and

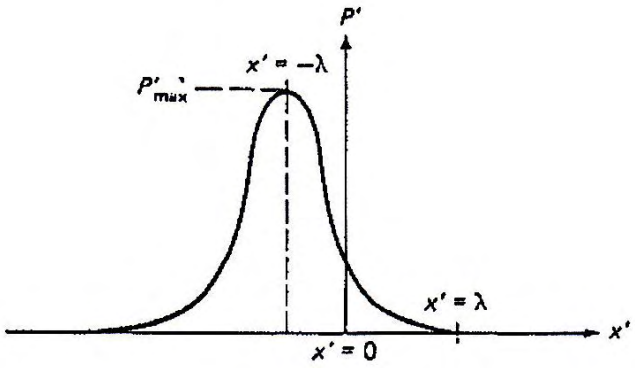

Figure 2.2. Schematic representation of the pressure distribution between the calenders as sketched by Middleman [1].

has the value of

$$p_{\max}'=\frac{3C(\lambda)}{2}\sqrt{\frac{R}{2H_o}} \tag{2.40}$$

where

$$C(\lambda)=\frac{1+3\lambda^2}{1+\lambda^2}\lambda-(1-3\lambda^2)\tan^{-1}\lambda \tag{2.41}$$

and becomes zero at $x'=\lambda$ where the polymer detaches from the calenders. At that point the pressure gradient vanishes. There is also another value of x' at which the pressure gradient vanishes and is seen to be at $x'=-\infty$. The pressure there is obtained if we set $x'=-\infty$ in Eq. 2.39 from which it is obtained

$$p'(x\to-\infty)=\sqrt{\frac{9R}{32H_o}}\left[\frac{1+3\lambda^2}{1+\lambda^2}\lambda-(1-3\lambda^2)\left(\frac{\pi}{2}+\tan^{-1}\lambda\right)\right] \tag{2.42}$$

The most reasonable assumption to be made here is

$$p'\left(x \to -\infty\right) = 0 \tag{2.43}$$

from which is followed that the dimensionless parameter λ has a finite value, namely

$$\lambda_o = 0.475 \tag{2.44}$$

and substituting that value in Eq. 2.43 then it can be seen that

$$\frac{H_f}{H_o} = 1 + \lambda_o{}^2 = 1.226 \tag{2.45}$$

and that the sheet thickness depends only on H_o. At that point it is noted that λ_o is the dimensionless leave–off distance when Eq. 2.43 is imposed. Thus, using the Lubrication Approximation Theory the final sheet thickness can be evaluated by measuring the distance H_o of the calenders at the nip region. The velocity and the pressure profiles can be derived with the assumption of infinite reservoir far upstream behind the nip region.

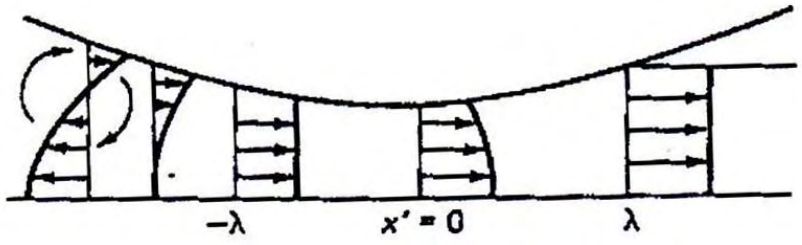

Figure 2.3. Recirculation flow pattern in the nip region. In the schematic only the half–region is shown from the top roller to the centerline [1].

Also the velocity profile can be easily obtained from Eq. 2.32 with the help of Eq. 2.36 and can be expressed as

$$u_x = 1 + \frac{3}{2}\frac{\left(1 - y'^2\right)\left(\lambda^2 - x'^2\right)}{\left(1 + x'^2\right)} \tag{2.46}$$

The velocity distribution across the gap through the calenders can be seen at Figure 2.3. Because of the pressure build-up at the nip region, there is a backflow component for $x' < -\lambda$ which is superimposed onto the drag flow component. Thus, near the entrance of the region between the calenders a recirculatory flow pattern develops. More on this topic will be discussed in a subsequent chapter.

2.3 Lubrication Approximation with the Power–Law Model

For the power–law viscosity model, the derivation of the pressure solution according to the LAT proceeds in a manner similar to that outlined earlier for the Newtonian fluid. For a power–law fluid, the shear stress τ_{xy} can be expressed in the following simple form

$$\tau_{xy} = m\left|\frac{\partial u_x}{\partial y}\right|^{n-1}\frac{\partial u_x}{\partial y} \tag{2.47}$$

where the absolute value sign on the velocity gradient term avoids the problem of taking a fractional root of a negative number.

From the Lubrication Approximation Theory solution for the Newtonian model we anticipate two flow regions, a region where the pressure gradient is positive $-\lambda < x' < \lambda$ and a region where the pressure gradient is negative $-\infty < x' < -\lambda$. Thus, integrating Eq. 2.12 by means of Eq. 2.47 separately for each region we have

$$u_x = U \pm \frac{1}{q}\left(\pm\frac{1}{m}\frac{dp}{dx}\right)^{\frac{1}{n}}\left[y^{\frac{n}{1+n}} - h(x)^{\frac{n}{1+n}}\right] \tag{2.48}$$

Introducing either of the above equations into the integrated equation of the conservation of mass (Eq. 2.14) and then solving for the pressure gradient, we have

$$\frac{dp'}{dx'} = -\left(\frac{2n+1}{n}\right)^n \sqrt{\frac{2R}{H_o}} \frac{\left(\lambda^2 - x'^2\right)\left|\lambda^2 - x'^2\right|^{n-1}}{\left(1+x'^2\right)^{2n+1}} \tag{2.49}$$

where the dimensionless pressure is the following

$$p' = \frac{p}{m}\left(\frac{H_o}{U}\right)^n \tag{2.50}$$

This equation is valid for both flow regions i.e. for where the pressure gradient is positive and for where the pressure gradient is negative. The pressure distribution is obtained by integration of Eq. 2.49, with the result

$$p' = \left(\frac{2n+1}{n}\right)^n \sqrt{\frac{2R}{H_o}} \int_{-\infty}^{x'} \frac{\left|\lambda^2 - x'^2\right|^{n-1}\left(\lambda^2 - x'^2\right)}{\left(1+x'^2\right)^{2n+1}} dx' \tag{2.51}$$

The computation of the integral in Eq. 2.51 must be performed numerically and the boundary condition $p'\left(x' \to \infty\right) = 0$ has been used.

It is simpler, computationally, to integrate Eq. 2.51 from λ (where $p' = 0$) to x' with the result

$$p' = \left(\frac{2n+1}{n}\right)^n \sqrt{\frac{2R}{H_o}} \int_{x'}^{\lambda} \frac{\left|\lambda^2 - x'^2\right|^{n-1}\left(\lambda^2 - x'^2\right)}{\left(1+x'^2\right)^{2n+1}} dx' \tag{2.52}$$

Then, the maximum pressure occurs at $x' = -\lambda$, so we may write

$$p_{\max}' = \left(\frac{2n+1}{n}\right)^n \sqrt{\frac{2R}{H_o}} \int_{-\lambda}^{\lambda} \frac{\left(\lambda^2 - x'^2\right)}{\left(1+x'^2\right)^{2n+1}} dx' \tag{2.53}$$

The dimensionless parameter λ can be obtained then from Eq. 2.51 taking into account the boundary condition which is described by Eq. 2.43. Thus λ_o is found from the following equation

$$0 = \int_{-\infty}^{\lambda_o} \frac{\left|\lambda_o{}^2 - x'^2\right|^{n-1}\left(\lambda_o{}^2 - x'^2\right)}{\left(1+x'^2\right)^{2n+1}} dx' \tag{2.54}$$

Note again here, that the notation λ_o is used to refer to that value of λ corresponding to the entrance condition $p'\left(x \to -\infty\right) = 0$. Then it can be calculated based on the dependence to the power–law index n as shown at Figure 2.4, where it is apparent that the effect of non–Newtonian behavior is to increase the sheet thickness.

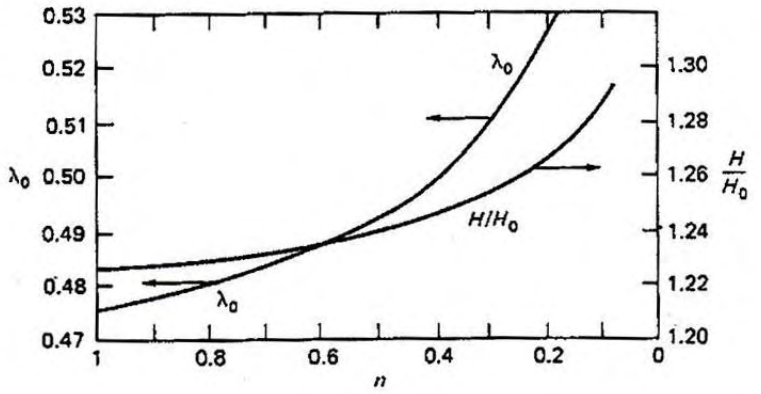

Figure 2.4. Thickness of the calendered sheet, in terms of λ_o or H/H_o, as a function of the power–law index n [1].

Once λ_o is determined from n, the maximum pressure may be found by the following equation

$$\frac{p'_{\max}}{\sqrt{2R/H_o}} = \left(\frac{2n+1}{n}\right)^n \int_{-\lambda_o}^{\lambda o} \frac{\left(\lambda_o{}^2 - x'^2\right)}{\left(1+x'^2\right)^{2n+1}} dx' \tag{2.55}$$

Chapter 3

Literature Survey of Calendering

A description of the calendering process as well as the hydrodynamic behavior of the fluid has been extensively studied and can be found in the literature. The earliest reported study concerning the calendering process was performed by Gaskell [5]. The analysis was based on the assumption that the diameter of the rolls is large enough compared to the gap between the calenders, thus approximating the flow as one dimensional. The developed analysis by Gaskell employed the flow of Newtonian fluids as well as Bingham plastic fluids.

Middleman [1] and McKelvey [6] summarized previous works on calendering and described a model for the calendering of Newtonian and power–law fluids. In his model they treated the flow with the Lubrication Approximation Theory simplifying the Navier–Stokes equations. By this, the analysis was restricted in unidirectional flow ignoring any fluid flow in the cross–machine direction (this direction is the same with the direction of the symmetry axis of the calenders). Although, such an approximation seems rational and holds for processes where the width of the sheet is very large, it is far from reality when the sheet is narrow. A theoretical approach on studying the calendering of power–law fluids was also showed by Brazinsky *et al* [7].

Alston *et al* [8] developed a one dimensional model to study the calendering process of non–Newtonian fluids which are described by a hyperbolic tangent model, they called it *tanh model*, exhibiting Newtonian behavior at high and low shear rates and a shear–thinning behavior at several intermediate shear rates. The authors also suggested

that extension of their work is the solution of a two–dimensional flow between the calenders.

Kiparissides and Vlachopoulos [9] studied symmetric and asymmetric calendering of Newtonian and non–Newtonian fluids numerically. In their model they simplified the Navier–Stokes equations by the Lubrication Approximation Theory and the resulting equations were solved by the finite element method. The pressure distribution along the centerline for a Newtonian fluid showed very good agreement at lower values of λ_o while at higher values there was a substantial deviation due to the coarse mesh they used consisting of long and narrow elements. The power–law viscosity model they also used in their analysis, produced results with the maximum pressure being substantially higher for Newtonian fluids than the non–Newtonian ones and the asymmetry (in calenders radii and speed) did not influence the results for the Newtonian fluid, but reduces the maximum pressures of non–Newtonian fluids as shown at Figure 3.1. Moreover, the same authors [10], used a finite–differences non–isothermal model to study the temperature distribution in the calendering process due to viscous dissipation phenomena, reporting two maxima of the temperature near the surfaces of the calenders caused by the large amount of shear.

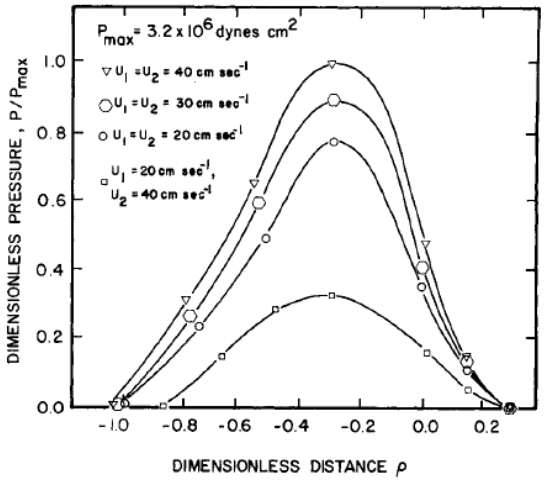

Figure 3.1. Pressure profiles along the centerline for calendering of a Power – Law fluid with n=0.25. The calenders (R=100 *mm*, H_o=0.1 *mm*) are rotating at different velocities [9].

Furthermore, Agassant [11,12], studied the flow between the calenders theoretically using a two–dimensional Finite Elements method, for rigid PVC, and also carried out experiments concerning the formed melt bank. In the computational method used, the streamlines in the calendering melt bank where calculated and the pressure distribution, in good agreement with the experiment, using the Lubrication Approximation. The numerical results, concerning the streamlines, are shown at Figure 3.2 in which there are two recirculation patterns. At Figure 3.3 is shown the flow pattern in the calender melt bank as observed experimentally with a huge vortex covering a large portion in the melt bank, while two smaller ones develop near the entering sheet and the nip region. It was also pointed out that when the calendering process is unstable (too large melt bank or too high output rate) the bank as well as the recirculating flow patterns flow in the third direction, and a spiral flow occurs. The spiral flow in the third direction and the existence of three vortices was firtsly observed by Unkrüer [13] and more results by his study will appear further on in the present thesis.

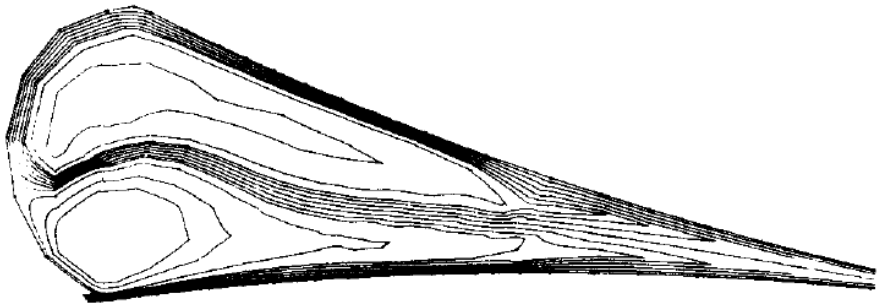

Figure 3.2. Numerically calculated streamlines in the melt bank [11, 12].

Figure 3.3. Experimental flow pattern in the melt bank of calendered PVC [11, 12].

Vlachopoulos and Hrymak [14] studied on a theoretical and experimental framework calendering of rigid PVC with an isothermal power–law model. The Lubrication Approximation method of solution with no–slip gave significantly higher pressure distribution in the nip region than the experiment. However, the experimental pressure was measured 80 *mm* from the center without reporting which was the experimental maximum pressure at the center. The Lubrication Approximation with slip predicted lower maximum pressure than the analysis with the no–slip approximation.

Moreover, Mitsoulis *et al.* [15,16] performed a two–dimensional, non–isothermal analysis with a purely viscous model without using the Lubrication Approximation Theory for Newtonian and power–law fluids (rigid PVC with data from Vlachopoulos *et al* [14]) by means of the Finite Elements method. In the analysis they captured the two recirculation flow patterns as it can be seen at Figure 3.4 and the temperature distribution for the region between the calenders including the melt bank as shown at Figure 3.5. Lubrication Approximation cannot predict the asymmetric recirculation patterns in the melt bank. The analysis also predicts the pressure distribution along the centerline. The numerical scheme used gave reasonable predictions for the pressure distribution especially when slip is included.

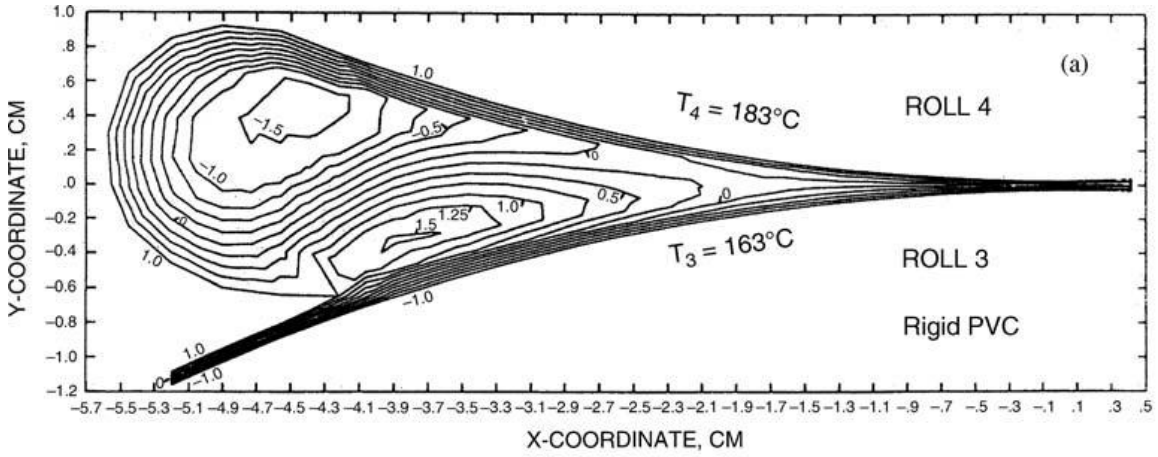

Figure 3.4. Calculated streamlines for the calendering of rigid PVC with data obtained from Vlachopoulos and Hrymak [14], indicating two recirculation regions [15,16].

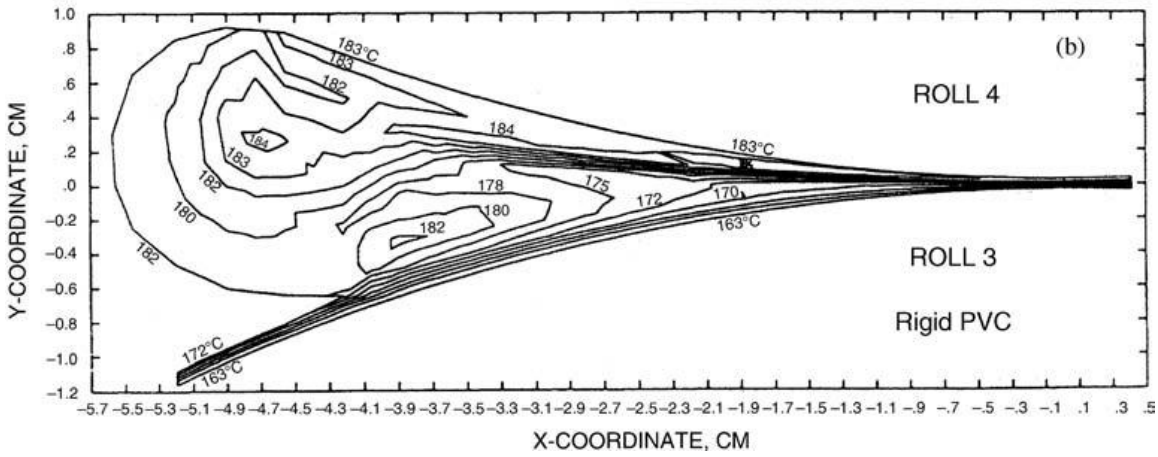

Figure 3.5. Calculated isotherms for the calendering process of rigid PVC [15,16].

More recent studies were carried out by Sofou and Mitsoulis [17, 18] for the calendering of viscoplastic and pseudoplastic materials using the Lubrication Approximation with no–slip and slip at the calenders surfaces but the results were of little importance.

Moreover, concerning the processing of carbon nanotubes with calendering a couple of studies are presented obtained from the literature [19, 20]. Kovacs *et al*. [19] studied the conductivity of Multi–Wall Carbon Nanotubes (MWCNT) by the help of a dissolver disk or additionally with a three roll calender. Specifically it was concluded that nanotube agglomerates were efficiently separated and dispersed through the calendering process due to the high shear forces they undergo in the nip region of the calender but this is not favourable for electrical conductivity applications. It was also pointed out that the flow forces exerted on the nanotubes caused attrition with a reduction of their aspect ratio from 1000 to 60. Moreover, Seyhan et al. [20] made a study which exhibits that a three–roll–milling process (a process which is very similar to calendering) is sufficient for the dispersion of carbon nanotubes in a thermoset polyester resin than other processes such as direct mixing.

In all the studies presented above, the calendering process was studied using two–dimensional numerical schemes (mostly Finite Elements Method) or one–dimensional

models such as the Lubrication Approximation. Of course, such approximations, give reasonable results concerning the pressure distribution along the centreline using no – slip or even slip assumptions at the calender surfaces. However, these studies neglect any 3D effects that take place, such as the spreading of the sheet from the entrance to the exit or the pressure distribution in the cross – machine direction as observed by Unkrüer [13]. The only known 3D study using numerical methods is by Luther and Mewes [21] who studied 3D effects in the melt bank when calendering non–Newtonian fluids. An extensive experimental analysis, as stated above, was carried out by Unkrüer [13]. More on this matter in calendering will be discussed further on in the present thesis.

Chapter 4

Finite Volume Method

Introduction

For all of the calculations at the present study the *OpenFOAM* (Open Source Field Operation and Manipulation) package is used which employs the Finite Volume Method (FVM) which subdivides the flow domain into a finite number of smaller control volumes. The transport equations are then integrated over each of these control volumes by approximating the variation of flow properties between mesh points with differencing schemes. The solver used in the present work is *simpleFoam* which is a steady – state incompressible solver that uses the FVM to simulate the flow of Newtonian and non – Newtonian fluids with the SIMPLE algorithm. The SIMPLE acronym stands for Semi – Implicit Method for Pressure Linked Equations and it was adopted by Patankar and Spalding [22] and it is actually a guess – and – correct procedure for the calculation of pressure. This section gives only a brief overview on the FVM [23,24], for a complete discussion on the FVM the reader is referred to *An Introduction to Computational Fluid Dynamics* by Versteeg and Malalasekera [25].

4.1 Discretisation of Continuous Operations

A computer can only process discrete quantities and therefore continuous quantities like space and time need to be discretised before processed. There are two main distinctive discretisation procedures that must be made in order to obtain the solution of a flow problem. These procedures are:

Spatial discretisation: Discretisation of the solution domain produces a computational mesh on which the governing equations of the flow are subsequently solved. The procedure can be split into two parts, discretisation of space and time. The discretisation of space for the Finite Volume Method used in this study requires a subdivision of the flow domain into control volumes (CV) or cells which do not overlap and completely fill the computational domain. It follows naturally that the boundary of the flow domain is decomposed into faces (f) connected to the cell next to it. The cell connected from the lower side of the face is called "owner" (P) and the cell connected from the higher side of the face is called "neighbor" (N) as shown at Figure 4.1. Generally, variables are stored at the cell centroids although they may be stored on faces or vertices. A cell is bounded by a set of flat faces with no limitation on the number of faces or their alignment, which can be called *arbitrarily unstructured*. The capability of OpenFOAM to discretise with arbitrary control volumes and produce *unstructured meshes* gives considerable freedom in mesh generation and appears to be useful in meshing complex geometrical configurations in three spatial dimensions.

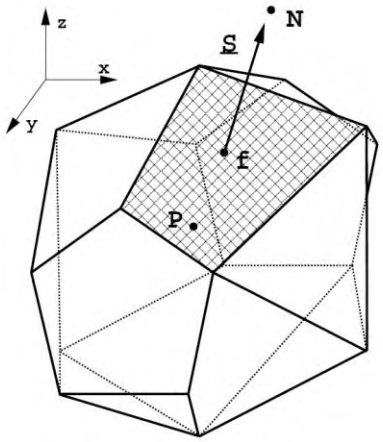

Figure 4.1. Arbitrary control volume [24]. (P) refers to the "owner" cell, (N) refers to the "neighbor" cell, (f) denotes the shaded area which is the face and ($\boldsymbol{S}$) is the face area vector.

Transport equations discretisation: The partial differential equations that are appropriate for certain cases must be discretised in order to be processed. OpenFOAM solves certain fields, like pressure and velocity, through a translation from the partial differential equations and the computational flow domain into a set of algebraic expressions. Specifically, the *simpleFoam* solver implements the Navier–Stokes

equations and supports the option to choose between turbulent or laminar flow. Since polymer melts are characterized by very low Reynolds numbers (i.e. 10^{-2} – 10^{-4}) their flow behavior is characterized as creeping and laminar. This was presented in a previous chapter. For that reason, it was chosen the option of laminar flow for the solver.

4.2 Governing and Constitutive Equations of the Solver

Fluid flow, in general, is mathematically described by the conservation of mass, momentum and energy. The *simpleFoam* solver, solves the equations presented below. These equations are the conservation of mass in a fully three dimensional form and the fully three–dimensional Navier–Stokes equation along with a constitutive equation that relates the stresses with the rates of strain. The study of any thermal effects and temperature distribution that take place in the calendering process is out of the scope of the present thesis, thus the energy equation was no solved. The general form of a conservation equation for a flow quantity ϕ if the flow is in steady state, is:

$$\nabla \cdot (\rho \mathbf{U} \phi) - \nabla \cdot (\rho \Gamma \nabla \phi) = S_{\phi} \tag{4.1}$$

where ρ is the density, $\mathbf{U}$= $\mathbf{U}(u_x,u_y,u_z)$ is the velocity, Γ is the diffusivity and S_{ϕ} is a source term. The transport equation for the conservation of mass, or continuity equation, is derived by setting $\phi = 1$ in Eq. 4.1 and not having any mass source terms. This subsequently leads to the following equation if incompressibility is taken into account

$$\nabla \cdot \mathbf{U} = 0 \tag{4.2}$$

The fully three – dimensional Navier – Stokes equation, neglecting any gravitational effects, and accepting that the flow is steady in time is the following

$$\nabla \cdot (\rho \mathbf{U}\mathbf{U}) = -\nabla p + \nabla \cdot \overline{\overline{\tau}} \tag{4.3}$$

where $\bar{\bar{\tau}}$ is the stress tensor, a second order tensor, which was showed in a previous chapter. The equation above, was presented in a previous chapter but in a slightly different form. In the solver the inertial term of the momentum equation is taken into account. In the following sections is presented how each term of the Navier–Stokes equation is discretised.

4.3 Discretised Equations

4.3.1 System of Equations

The discretisation and linearization procedure outlined in the previous sections produces a linear algebraic equation for each control volume. The exact form of these linear algebraic equations depends on the governing equation and the discretisation practices used, but they can be re–written in a generic formulation, in matrix form such as below

$$[\mathrm{A}][\phi] = [b] \tag{4.4}$$

where [A] is a tridiagonal matrix in the form below

$$\mathrm{A} = \begin{bmatrix} \mathrm{I} & C & & & & \\ -C & \mathrm{I} & C & & & \\ & -C & \mathrm{I} & C & & \\ & & -C & \mathrm{I} & C & \\ & & & -C & \mathrm{I} & C \\ & & & & -C & \mathrm{I} \end{bmatrix} \tag{4.5}$$

[x] is the column vector of dependent variable, in the form below

$$\phi = \begin{bmatrix} \phi_1 \\ \phi_2 \\ \vdots \\ \phi_{\mathrm{N}} \end{bmatrix} \tag{4.6}$$

and [b] is the source vector

$$b = \begin{bmatrix} b_1 \\ b_2 \\ \vdots \\ b_N \end{bmatrix} \tag{4.7}$$

The solution of this system approximates the solution to the original equations at some pre–determined locations in space (and time for unsteady flows). The numerical methods for the solution of the above type of matrix fall into two main categories, direct methods and iterative methods. Direct methods involve direct solution of Eq. 4.4 and require inversion of the matrix [A]. Iterative methods, start with an initial guess and then continue to improve the current approximation of the solution until some tolerance is met. For direct methods, the number of operations necessary to reach for the desired solution, scales approximately with the cube of the number of equations (or the unknowns), thus making them computationally very expensive especially for large systems. On the other hand, the total number of operations required by iterative methods, typically of the order of N per iteration cycle, cannot be predicted in advance. Stronger still, it is not possible to guarantee convergence unless the system of equations satisfies fairly exacting criteria. The main advantage of the iterative methods is that only non–zero coefficients of the equations need to be stored in memory thus, making these methods for solution more economical computationally.

On a specific number of iterations, for iterative methods, the solution will be ϕ^n, and it will not fully satisfy Eq. 4.4, in the sense of a non–zero residual $\boldsymbol{r}^n$. Mathematically, this can be expressed as

$$[\mathrm{A}][\phi]^n = [b] - [r]^n \tag{4.8}$$

The aim is to minimize the value of the residual. If that value is small enough, then it can be approximated that

$$[\phi]^n \approx [\phi] \tag{4.9}$$

In the present study the *conjugate gradient* method is used in order to reach for the solution after a certain number of iterations which was introduced by Hestenes and Stiefel [26].

4.3.2 Linearization of the Navier – Stokes Equations

In the present study each term of the Navier – Stokes equation (Eq. 4.3) is discretised. *Finite volume* (FV) discretisation of each term is formulated by integrating the terms of the equations over a cell volume *V* (control volume). If not all, at least most, spatial derivatives are converted to integrals over the cell surface *S* that bounds the volume by means of Gauss's theorem

$$\int_V \nabla \phi = \int_s d\mathbf{S}\phi \tag{4.10}$$

where $\boldsymbol{S}$ is the surface area vector and ϕ can represent any variable. The calculated values of pressure (p) and velocity (**U**) are stored at the same nodal points which are actually the centroid of each cell. Such an arrangement of the computational domain is called *collocated* arrangement. OpenFOAM utilizes such type of arrangements, like in the present study.

The Diffusive Operator

The diffusion term is integrated over a control volume and linearised as follows

$$\int_V \nabla \cdot (\mu \nabla \mathbf{U}) dV = \int_S \mu \nabla \mathbf{U} d\mathbf{S} = \sum_f \mu_f \mathbf{S}_f \cdot (\nabla \mathbf{U})_f \tag{4.11}$$

where μ is the viscosity for a Newtonian fluid and the index *f* refers to the face interpolated values. The previous can be discretised when the length vector **d** between the

centre of the cell of interest *P* and the centre of a neighboring cell *N* is orthogonal to the face

$$\mathbf{S}_f \cdot (\nabla \mathbf{U})_f = |\mathbf{S}_f| \frac{\mathbf{U}_N - \mathbf{U}_P}{|\mathbf{d}|} \tag{4.12}$$

In the present work, the term was evaluated using *Gaussian integration* which requires the interpolation of values from the cell centroid to the face centers. The interpolation scheme used is *central differencing* for the μ_f and the surface normal gradient $\nabla \mathbf{U}$, which is second order accurate. As explained in detail in Breuer [27], a second–order accurate scheme is even appropriate for LES of turbulent flows and consequently is reliable for the simulation of laminar flows carried out within the present study. The same scheme was also used by Biswas *et al*. [28] who investigated laminar and creeping flows in a backward–facing step at low and moderate Reynolds numbers.

The Convective Operator

The convection term, as previously, is integrated over a control volume and linearised as shown below using *Gaussian integration*

$$\int_V \nabla \cdot (\rho \mathbf{U}\mathbf{U}) dV = \int_S d\mathbf{S} \cdot (\rho \mathbf{U}\mathbf{U}) = \sum_f \mathbf{S}_f \cdot (\rho \mathbf{U})_f \mathbf{U}_f = \sum_f F \mathbf{U}_f \tag{4.13}$$

where *F* in Eq. 4.13 represents the mass flux through the face. The face field $\mathbf{U}_f$ can be evaluated using a variety of schemes. In the present work, the used interpolation scheme is the *upwind differencing* which is first order accurate but bounded and determines ϕ_f from the direction of flow. That scheme was used for stability reasons.

The Gradient Operator

The gradient term, which is described here, is an explicit term. Usually it is evaluated using *Gaussian integration* (as in the present study) which requires the interpolation of values from the control volume centroid to the face centers. The interpolation scheme

used is *central differencing*. Therefore, applying Eq. 4.10 to the volume integral we have the following

$$\int_V \nabla p dV = \int_S d\mathbf{S} \cdot p = \sum_f \mathbf{S}_f p_f \tag{4.14}$$

where p_f is the value obtained from the interpolation and $\mathbf{S}_f$ is the area of the surface that bounds the control volume. There are more ways to evaluate the gradient term. For more information the reader is referred to the OpenFOAM Programmer's Guide [29] and the User's Guide [23].

4.4 Numerical Setup

For the simulations, the *simpleFoam* solver of the OpenFOAM package was employed which is a steady – state solver for incompressible, viscous fluids. The flow is assumed to be laminar. For the pressure calculation, a pressure–correction equation taking mass conservation expressed in Eq. 4.2 into account was solved iteratively along with Eq. 4.3. The entire procedure follows the well–known SIMPLE algorithm proposed by Patankar and Spalding [22]. The solution of the algorithm was met until a desired tolerance was reached. It was assumed the tolerance for the pressure and the momentum equation to be 10^{-7} both for the Newtonian and the Generalized Newtonian Fluid.

Chapter 5

Calendering Validation with OpenFOAM

Introduction

In order to validate the *simpleFoam* solver against the approximated analytical solutions, a computational flow domain is constructed based on an arbitrary geometry which is rather common in the commercial calendering machines. Firstly, it was tested a geometry with a Newtonian fluid and further on with the Generalized Newtonian Fluid model for the same geometry. The approximate geometry along with the boundary conditions of the Lubrication Approximation Theory, pose a two–dimensional solution but on a three–dimensional geometry. For the sake of saving computational time, it could be constructed a two–dimensional geometry. However, the present three–dimensional geometry will be, in subsequent chapter, the basic computational flow domain on which the three dimensional effects of calendering will be studied after small modifications in the flow domain.

5.1 Newtonian Fluid

5.1.1 Flow Domain Geometry

At this chapter the flow behavior of a simulated Newtonian isothermal fluid between the calenders is studied using OpenFOAM and is directly compared to the analytical solution. The flow domain generated with the software is presented at Figure 5.1 and Figure 5.2 and the geometry dimensions are shown at Table 5.1. The x–axis will

represent the machine direction (that axis will always be parallel to the centerline shown at Figure 2.1). The y–axis will represent the vertical distance from the top to the botton surface of the calenders and finally z–axis will represent the cross – machine direction (which means that z–axis is parallel to the symmetry axis of each calender). The values for the geometry used are arbitrary but close enough to the dimensions of commercial calenders.

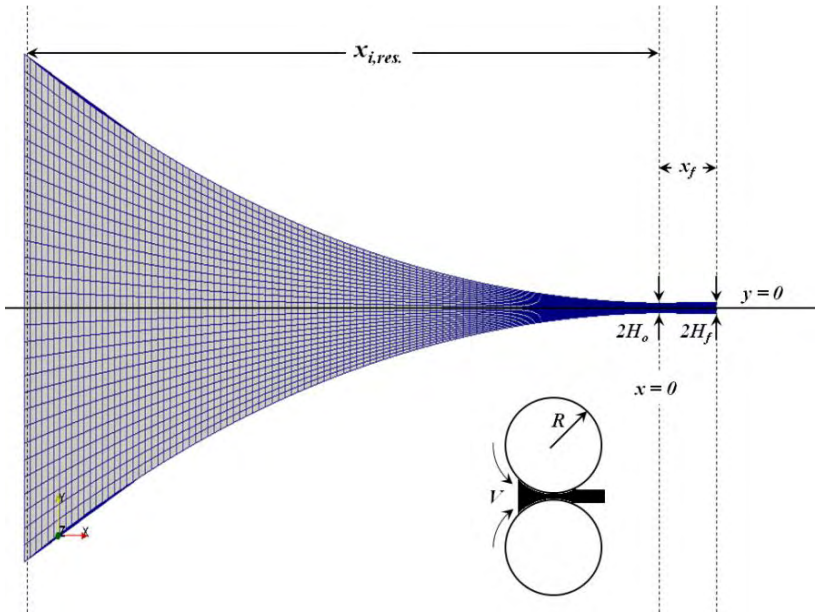

Figure 5.1. Side view (cross–section) of the computational flow domain, for $x_{i,res.}$ = -100.00 mm

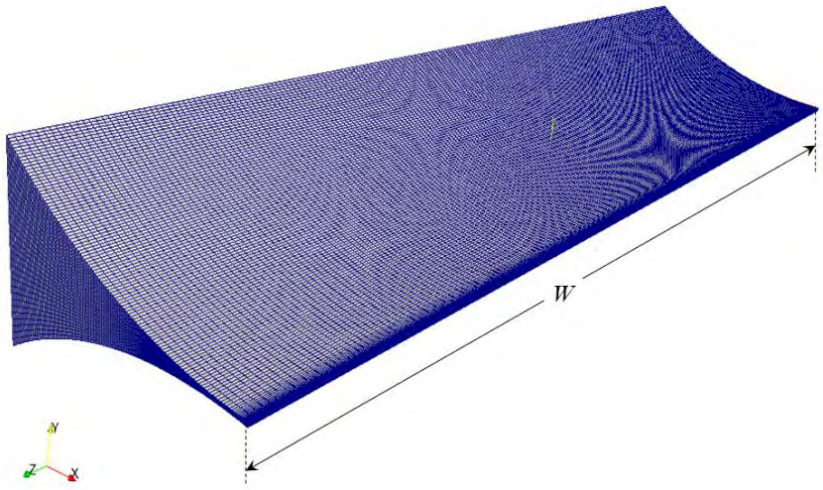

Figure 5.2. Inclined view of the computational flow domain for $x_{i,res.}$ = -100.00 mm.

The results of the present simulations are based on the pressure distribution along the centerline (*x*–direction), which is the machine direction, and then they are directly compared to the analytical solution from the Lubrication Approximation Theory. The analytical solution was obtained using the CALENDERCAD [29] which solves the Lubrication Approximation equations with a fourth–order Runge–Kutta formula and can calculate the pressure distribution along the centerline as well as the approximated point where the sheet detaches from the calenders with no–slip.

Table 5.1.

Dimension of the Geometry	**Value**
Nip gap ($2H_o$)	1.000 mm
Final sheet thickness ($2H_f$)	1.226 mm
Roller diameter (D)	400.000 mm
Roller velocity (V)	0.0334 m/s
Roller width (W)	500.000 mm
Attachment point from Lubrication Approx. (x_i)	-40.000 mm
Detachment point (x_f)	6.72 mm
Infinite reservoir point ($x_{i,res.}$)	-100.000 mm
Flow rate (Q)	55 kg/hr
Viscosity (μ)	15000 Pa·s
Density (ρ)	1000 kg/m^3

As far as the detachment point is concerned, the adopted value was the one derived from Eq. 2.42 of the Lubrication Approximation theory with $\lambda_o = 0.475$ being the dimensionless detachment point (or $x_f = 6.72\ mm$) and $H_f / H_o = 1.226$ as it seems a very reasonable approximation. The geometry of the computational flow domain is calculated through the following simple equation by which the shape of the calenders is cylindrical (and thus, their cross–section circular)

$$\mathrm{H}(x) = H_o + R - \left(R^2 - x^2\right)^{1/2} \tag{5.1}$$

where *H(x)* is the half gap between the rollers at each position *x*. However, Middleman [1] refers that for positions which are relatively close to the nip region, in order to

simplify his analysis with the Lubrication Approximation, the surfaces of the calenders can be approximated as a parabolic shape. Thus Eq. 5.1 is approximated as

$$\mathrm{H}(x) = H_o\left(1 + \frac{x^2}{2H_oR}\right) \tag{5.2}$$

Since, in the present study an infinite reservoir is assumed upstream which is located far behind the nip region, the only reasonable approximation for the construction of the computational domain was to treat the calenders surface as circular and use 5.1. A similar procedure is followed by Mitsoulis [17,18] for the numerical simulation of calendering viscoplastic fluids using the Finite Element Method. Following Middleman's [1] approach it is also assumed in the present study that far behind the nip region the feeding is done from an infinite reservoir. It was also approximated that pressure becomes zero (p=0, $x \rightarrow -\infty$) far away behind the nip region. The computational domain shown at Figures 5.1 and 5.2 does not necessarily represent the true physical boundaries of the process, since in the real process the feeding is done with a sheet of finite thickness and a melt bank appears near the attachment point. The shape of the free surface that describes the melt bank is however, beyond the scope of this study. The approach of the computational domain adopted in the present study is done for the sake of imposing the boundary conditions as described by the Lubrication Approximation and for further comparison with the analytical solution.

5.1.2 Boundary Conditions

The flow domain consists of regions that coincide with the boundaries of the physical domain. To correctly simulate the conditions between the two rollers, boundary conditions at all boundaries also need to be specified. Below the used boundary conditions of the Newtonian case study are shown following the same notation as in [23,30] and the boundaries are shown at Figure 5.3. In the formulation below the vector **n** denotes the direction normal to the boundary.

- *Top and bottom rollers*
  - Pressure: Normal gradient of pressure is zero, $\frac{\partial p}{\partial \mathbf{n}} = 0$
  - Velocity: no – slip at the roll surface (tangential velocity u_t=V, normal velocity u_n=0)

- *Sides*
  - Pressure: Normal gradient of pressure is zero, $\frac{\partial p}{\partial \mathbf{n}} = 0$
  - Velocity: Normal gradient is zero, $\frac{\partial \boldsymbol{U}}{\partial \mathbf{n}} = 0$

- *Outlet*
  - Pressure: Fixed value, p = 0
  - Normal gradient of velocity is zero, $\frac{\partial \boldsymbol{U}}{\partial \mathbf{n}} = 0$

- *Inlet*
  - Pressure: Fixed value, p = 0
  - Velocity: Known flow rate $Q = \rho \cdot u_t \cdot W \cdot (2H_i)$

where $2H_i$ is the distance between the rollers at the inlet.

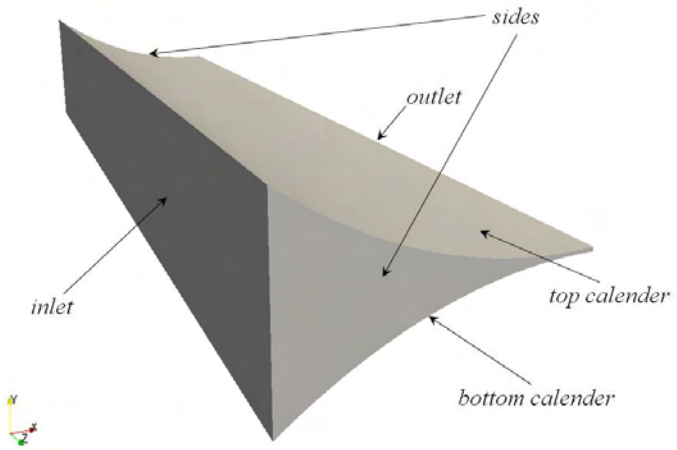

Figure 5.3. Side view of the computational domain with notation of each boundary.

Some comments concerning the boundary conditions should be made to this point. First of all it was approximated that the inlet boundary is far away from the nip region of the calenders and the material is fed continuously from an extruder or any other device. The fluid flow at the inlet is not delayed by any means of obstacles (i.e. there is not any pressure build–up) thus, the only reasonable assumption that can be made is to set the pressure equal to zero as this boundary is in contact with the atmosphere. Concerning the velocity boundary condition at the same boundary, it is assumed that the flow rate is known with a constant velocity profile. For the velocity boundary at the exit, where the detachment point lies, it is accepted that the gradient of the velocity normal to the boundary is zero, as presented above. This implies fully developed flow along the normal direction. On that same boundary, it was imposed that p=0. In Lubrication Approximation according to numerous publications such as Middleman [1], McKelvey [6], Mitsoulis [15-18] and Tanner [31] the boundary condition imposed at the detachment point is $p=dp/dx$=0. In a similar, almost convenient manner, and since that boundary is actually a free surface, it is treated as a surface with p=0 (as it is assumed that is in contact with the atmosphere) and zero gradient for the velocity, considering that in the present study the detachment point is obtained from the Lubrication Approximation. By this it is implied that from this boundary there is outflow. Concerning the side boundaries, it was approximated that there is no spreading of the sheet in the z–direction (cross–machine direction) and the prescribed boundary conditions basically assume calenders with infinite length along that direction and in that the effects along the z–direction are not taken into account for the present chapter.

5.1.3 Results and Discussion

The results obtained from simulations for the pressure distribution along the centerline are presented at Figure 5.4 for a Newtonian fluid with the well know bell–shaped curve. As it was previously discussed, it was assumed that far behind the nip region there is an infinite reservoir of the material where it is assumed that p=0 as described by the Lubrication Approximation Theory. The question that arises here is how much far that point should be. At first it was assumed that p=0 at x_i =-40.00mm (value obtained from CALENDERCAD [29]) and at the second simulation that p=0 at $x_{i,res.}$=-

100.00 mm as shown at Figure 5.4. Also, based on the analytical solution by CALENDERCAD [29] at the attachment point the pressure is not taken to be zero but it has a small pressure build–up. This might be due to the approximations the software performs to calculate the attachment point. So, the location of $x_{i,res.}$=-100.00mm seems as a rational approximation as the numerical results exhibit very good matching with the analytical solution. The maximum pressure reported by the Lubrication Theory is P_{max}=10.77MPa and the simulation gives P_{max}=10.75MPa. The simulations were performed for a flow domain filled with 225000 cells and the detachment point was at 6.72 mm and calculated from the Lubrication Approximation Theory.

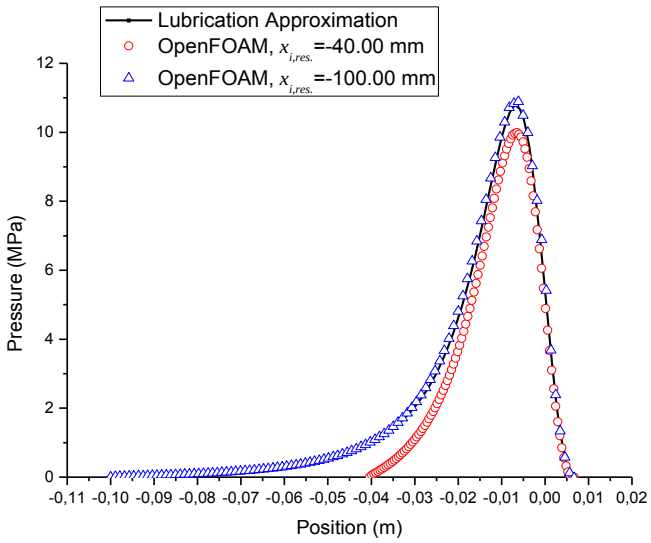

Figure 5.4. Pressure distribution along the centerline with p=0 at x_i=-40.00 mm and at $x_{i,res.}$=-100.00 mm. The pressure is plotted at W/2 (middle section).

Furthermore, the behavior of the numerical solution with different levels of refinement of the computational flow domain was investigated as shown at Figure 5.5. For 2000 cells the solution shows a relatively small oscillation (wiggles) around the point of the maximum pressure and this is caused due to the poor domain discretisation, whereas for the 27750 cells the numerical solution was good enough to the one of 225000 cells.

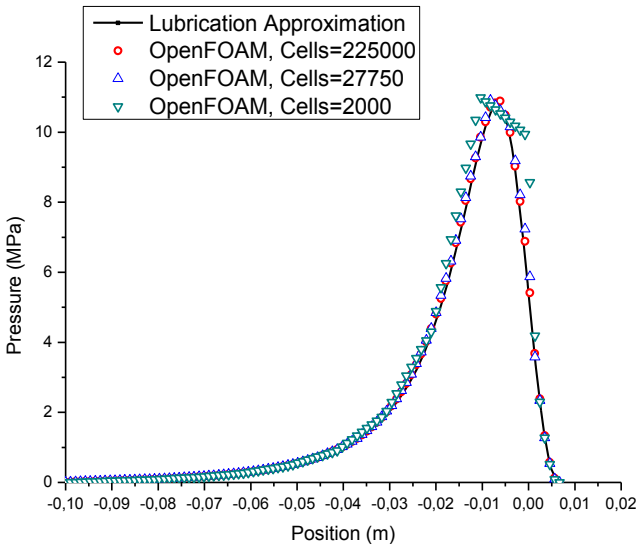

Figure 5.5. Pressure distribution along the centerline for three different levels of mesh refinement at *W*/2.

At Figure 5.6 the effect of displacing the detachment point 0.2 *mm* and 1 *mm* is exhibited. In the curves of Figure 5.6 we show how the displacement of this point effects the shape of the pressure distribution along the centerline as well as its peak value. This is done since in practice, even Newtonian fluids tend to slip at the exit of a die or a channel [34,35], which means that the exact point or line of detachment is difficult to predict. The analytical solutions derived in a previous chapter, do not take into account any slip phenomena that occur at the surfaces of the calenders and the value for the detachment point is obtained through various simplifications which were presented earlier in the present section. At first, we displace the detachment point by approximately 0.2 *mm* backwards and then at 0.2 *mm* forward. The shape of the bell–shaped curve is not altered at all with the maximum pressure preserved to P_{max}=10.75 *MPa* approximately. By this, it can be concluded that the exact location of the detachment point is not a critical parameter in estimating the maximum pressure as well as the shape of the pressure curve. For larger displacements of the detachment point, of the order of 1 *mm* backwards and forwards, the plotted pressure profile had the same distribution as in the previous simulations and the maximum pressure was P_{max}=10.75 *MPa* for the displacement at x_f =5.72 *mm* and P_{max}=10.71 *MPa* for the displacement at x_f=7.72 *mm*. Therefore, the above

conclusion can be extended for uncertainty in the location of the detachment point of the order of ±1 *mm*.

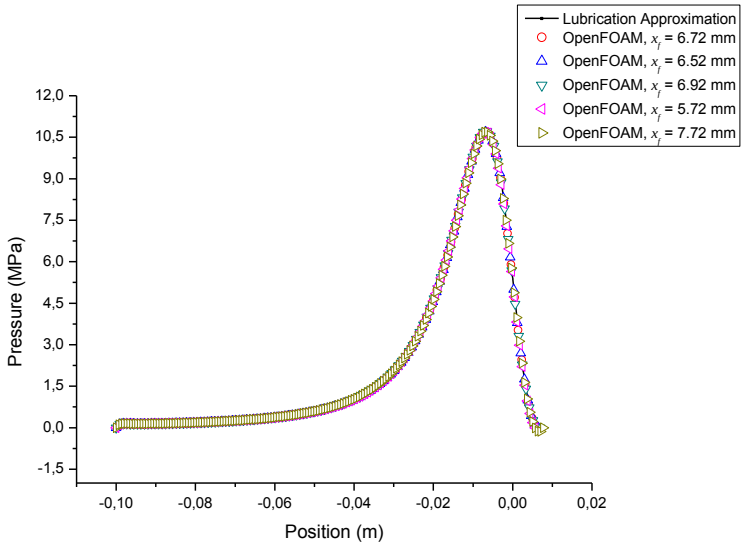

Figure 5.6. Pressure distribution concerning the displacement of the detachment point. The Lubrication Approximation gives a detachment point at x_f =6.72 mm. The infinite reservoir is assumed to start at $x_{i,res.}$= -100.00 mm. All the values are plotted at *W*/2 (middle section).

At Figure 5.7 and Figure 5.8 the velocity field and the streamlines are shown respectively for a flow domain of 760000 cells and for $x_{i,res.}$=-100.00 *mm* and x_f =6.72 *mm*. The numbers of cells for that simulation was increased to 760000 cells because we were interested to capture the details of the flow regime. The results show clearly two symmetric to the centerline recirculation patterns, something that has been mentioned in numerous publications discussed in a previous chapter for calendering of Newtonian fluids. These vortices are a result of the drag induced flow of the Newtonian fluid between the calenders and the back–flow due to the pressure build–up at the nip region. From Figure 5.9, it can be concluded that the maximum velocity of the flow is developed in the nip region. Due to the fact that the distance between the calenders in the nip is the minimum, the velocity of the material increases. Such velocity behavior is observed in entry flows where the material enters to a small tube from a large reservoir. Extensive simulations on the entry flows were made by Mitsoulis [32] in his doctorate thesis.

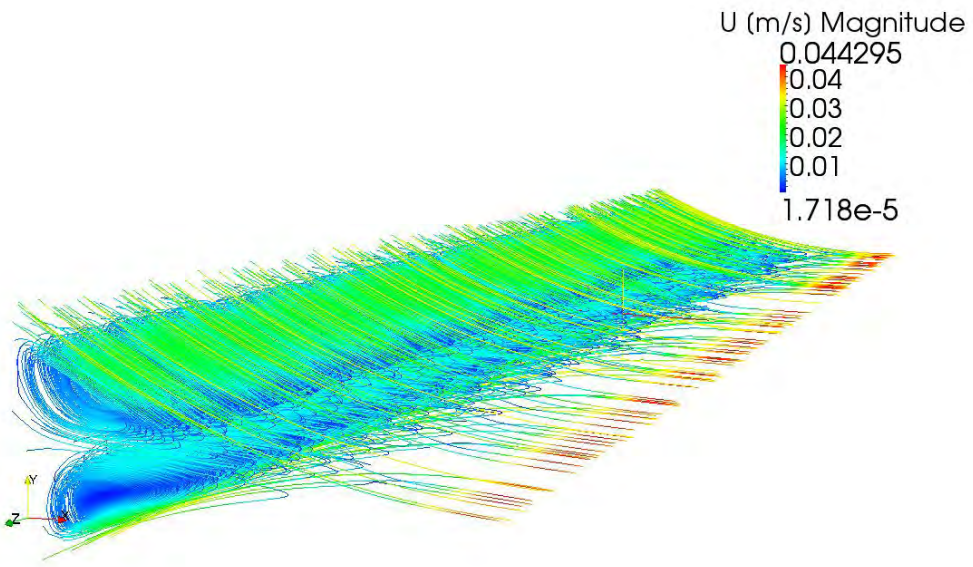

Figure 5.7. Streamlines for a flow domain of 760000 cells. $x_{i,res.}$ = -100.00 *mm* and x_f =6.72 *mm*.

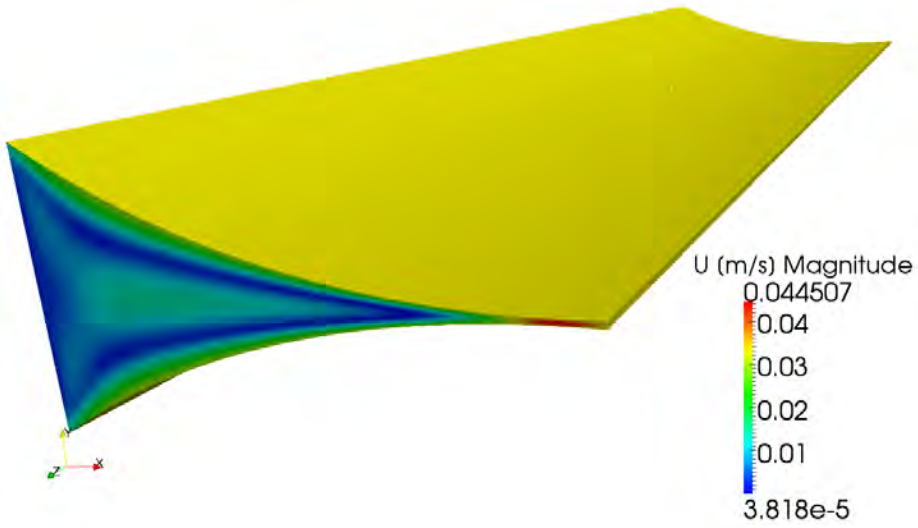

Figure 5.8. Variation of fluid speed along the flow domain of 760000 cells. $x_{i,res.}$ = -100.00 *mm* and x_f = 6.72 *mm*.

Furthermore, it can also be concluded that the outlet boundary (which is marked in Figure 5.3) appears to have the same velocity with the velocity of the calenders implying that the Newtonian fluid leaves the point of detachment with the same velocity.

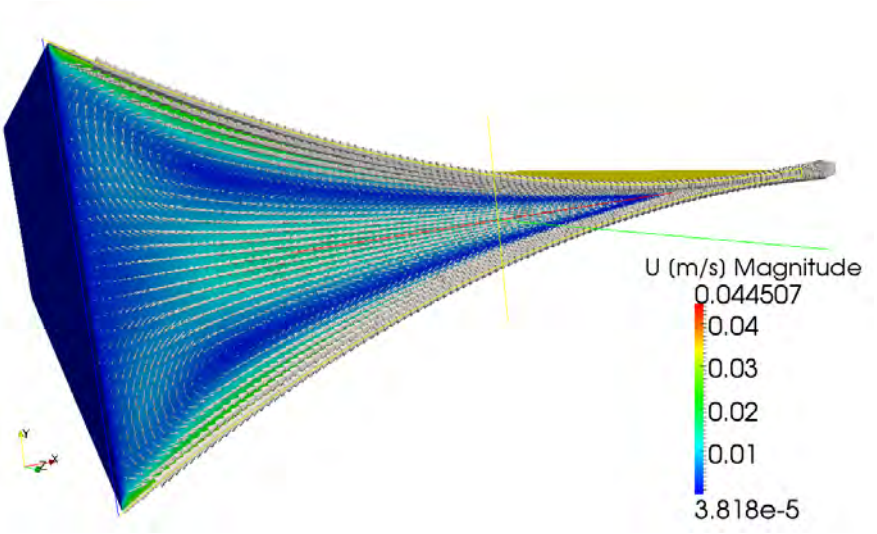

Figure 5.9 Velocity vectors for a flow domain of 760000 cells. $x_{i,res.}$ = -100.00 *mm* and x_f = 6.72 *mm*. The vectors are plotted at a computational domain slice located at *W*/2.

Middleman [1] reports such a behavior in his study with the analytical approximation, where it is assumed that after the detachment point the velocity is constant (*plug flow*) and equal to the velocity of the calenders. This is validated and further on the present study by calculating the velocity profile at the exit boundary. However, in Mitsoulis [33] study it is reported that the material at the exit leaves the rollers with a little lower velocity. Finally, the velocity vectors are plotted on a slice of the computational domain in the middle region (located at *W*/2) as shown at Figure 5.9.

Moreover, at Figures 5.11, 5.12 and 5.13 the velocity components and their magnitude in the y–direction are plotted for different positions as showed at Figure 5.10. It can be seen at Figure 5.11 that at *x*=-70.00 *mm*, u_x is maximum near the calenders and near the centerline decreases, taking negative values. The negative values imply backflow and this is why the recirculation patterns occur. The velocity component in the y–direction, u_y, appears to be maximum near the surfaces of the calenders and holds small to zero values for a region close enough to the centerline. This implies, that near the centerline the dominant velocity component is in the x–direction. The velocity in the z–direction, u_z, is approximately zero something which was anticipated based on the set of boundary conditions at the two side boundaries. The velocity magnitude exhibits maximum values near the surfaces of the calenders, and as we move to the centerline

from the calender surfaces, it decreases and finally exactly on the centerline increases again. The increase on the centerline is due to the occurring backflow and since the velocity magnitude is always a positive value, its values lie on the positive side of the axis, resulting in $U_{mag.}$ profile showed at Figure 5.11. Similar velocity profiles are found at x=-30.00 *mm*, with the maximum absolute value of u_x being smaller than the location of x=-70.00 *mm*.

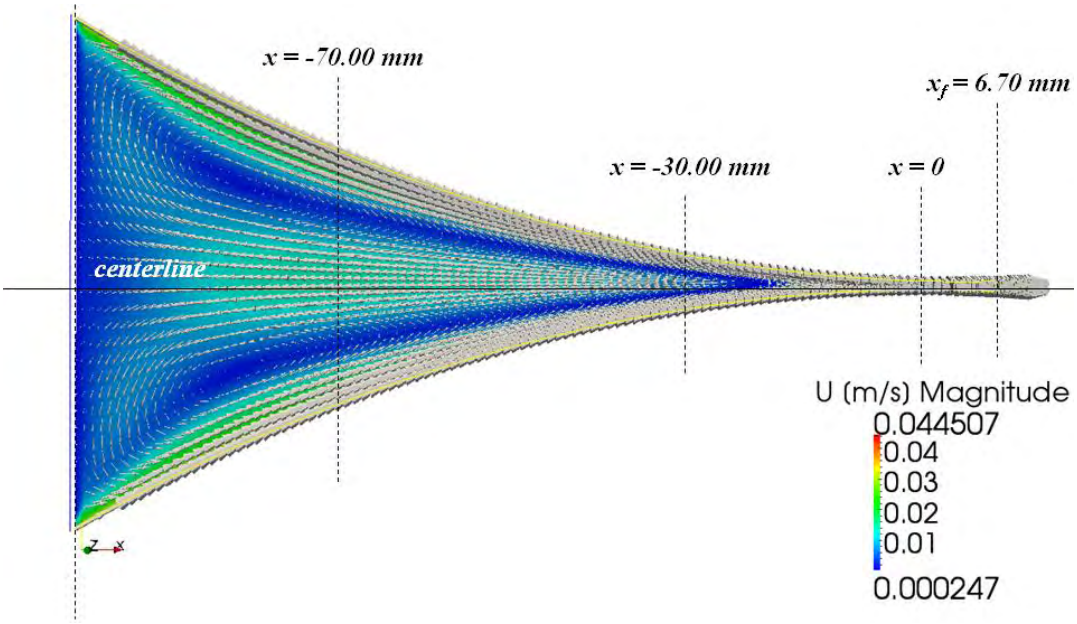

Figure 5.10. Cross–sectional area with the velocity magnitude field and velocity vectors with indications at four different arbitrary locations normal to the xz plane.

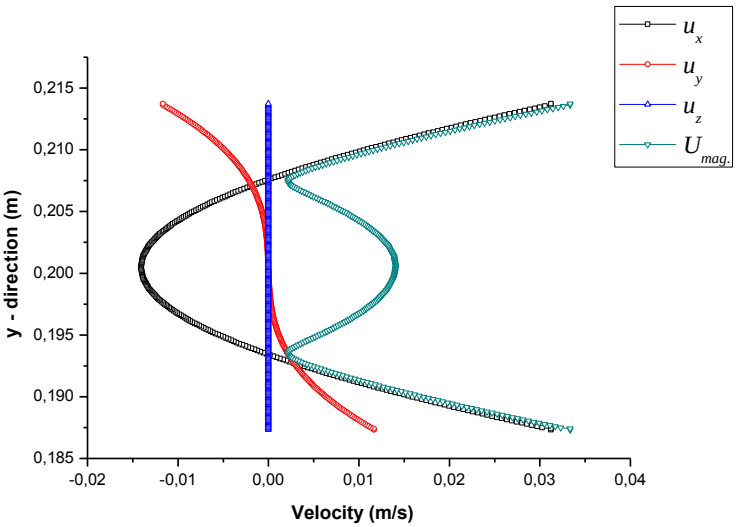

Figure 5.11. Velocity components profiles and velocity magnitude profile at x=-70.00 mm.

This means that as the fluid progresses to the exit the recirculation effects are becoming less intense, something which can be seen at Figures 5.13 and 5.14. At Figure 5.13 the profiles of u_x and $U_{mag.}$ match, thus the dominant flow occurs in the x–direction and since the velocity profile is parabolic with positive values, there is not any recirculatory patterns at that location. The velocity components at the other directions are approximately zero. For the exit boundary, at x_f =6.72 *mm* the velocity profile exhibits small variations but it can be considered as flat as it can be seen at Figure 5.14. This is the result of the velocity applied boundary condition at the exit, by which the velocity gradient normal to the boundary is zero and as in the previous location u_x and $U_{mag.}$ curves match. The matching of the curves implies that at the nip region as well as after the nip the flow can be considered as one dimensional as the dominant velocity component lies in the *x*–direction. The present results, validate the behavior of the velocity presented by previous studies, namely in Middleman [1], Gaskell [5] and Mckelvey [6].

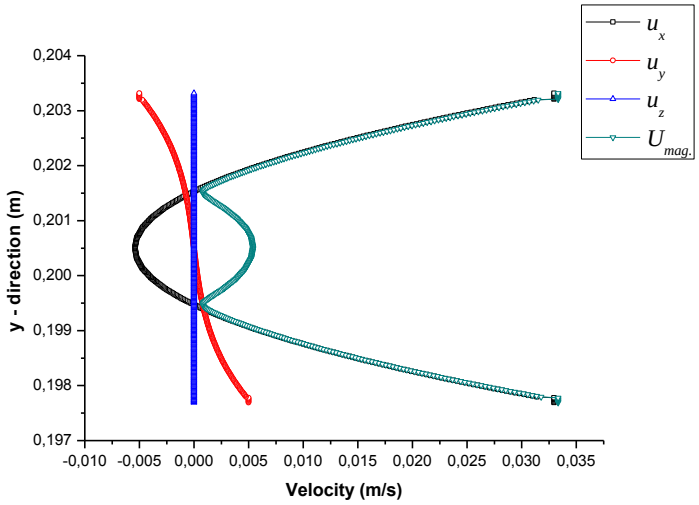

Figure 5.12. Velocity components profiles and velocity magnitude profile at *x*=-30.00 mm.

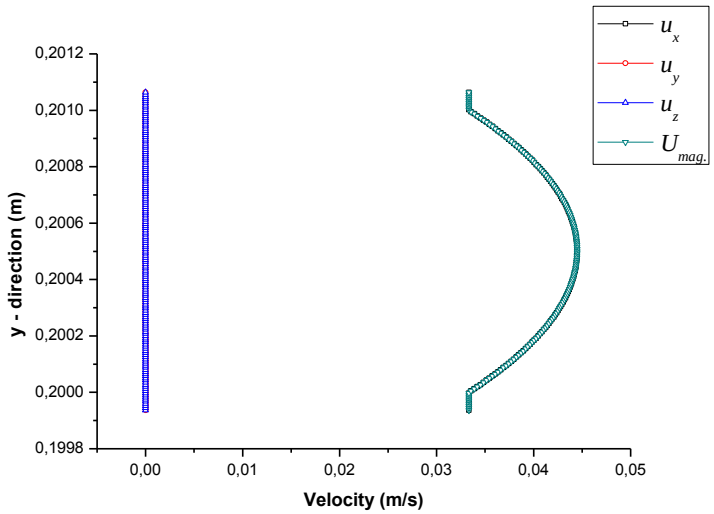

Figure 5.13. Velocity components profiles and velocity magnitude profile at *x*=0 (nip region).

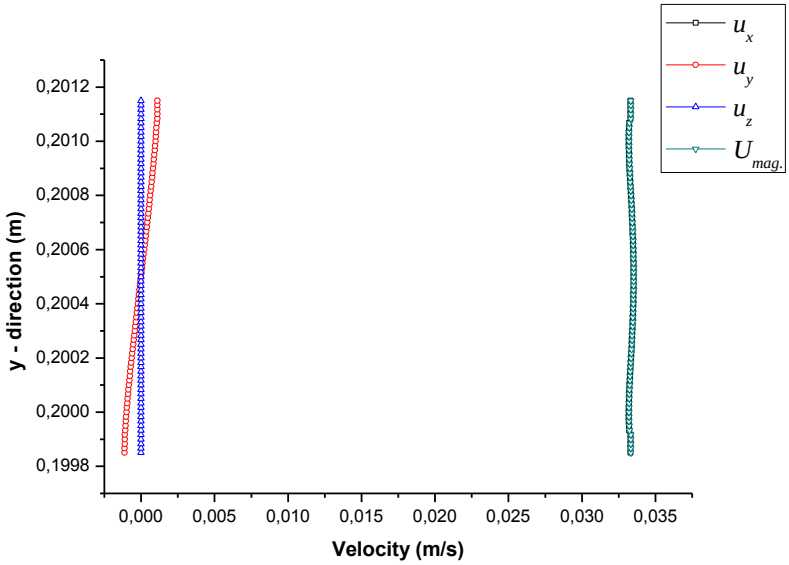

Figure 5.14. Velocity components profiles and velocity magnitude at *x*=6.72 mm (exit boundary).

.

5.2 Generalized Newtonian Fluid Model

5.2.1 Flow Domain Geometry and Boundary Conditions

At the present chapter the pressure distribution along the centerline for a non–Newtonian fluid is investigated neglecting any thermal phenomena that physically take place in the process. Thus the energy equation is not solved in the present study. The validation of the simulations is done based on the work of Vlachopoulos and Hrymak [14]. For that reason, and again assuming that there is an infinite reservoir far behind the nip region, we set the point of $x_{i,res.}$=-100.00 mm which will be the location of the inlet boundary for the computational flow domain. In the previous Newtonian study the equations of the Lubrication Approximation Theory are solved analytically and the value of the detachment point is calculated exactly. However, for the power–law fluid the Lubrication Approximation is applied through numerous approximations and the value of the detachment point is more difficult to be calculated analytically as with the power–law viscosity model an extra parameter is inserted in the equations (that is power–law index n). A recent publication of Mitsoulis [36] concludes that the exact location of detachment (and attachment point) in calendering still remains an unresolved issue. The detachment point according to the Lubrication Approximation is obtained analytically to be at x_f =4.37 mm with the assumption that the feeding is done from an infinite reservoir far upstream. In the present study, we accept x_f =4.37 mm as a sufficient initial guess of the detachment point. The feeding of the material is approximated to be through an infinite reservoir that comes off an extruder or any other continuous polymer processing machinery. Concerning the viscosity model, the power–law viscosity is utilized (Eq. 2.23) with m=46120 $Pa \cdot s$ and n=0.34 as shown at Table 5.2 below. Although there is an exponential or Arrhenius type dependence of viscosity with the temperature, in the present study we assume that the viscosity is no affected by temperature. Moreover, as in the simulations for the Newtonian fluid, the surfaces of the calenders are assumed to be cylindrical (Lubrication Approximation Theory assumes parabolic calenders surfaces) and the polymer cannot slip. Since we examine the pressure distribution only in the x–direction, it seemed rational to utilize the boundary conditions of the previous study with the Newtonian fluid.

5.2.2 Results and Discussion

The first simulation performed was to test the geometry given in Table 5.2 with a Newtonian fluid and the detachment point was known a priori from the Lubrication Theory to be x_f =4.37 mm. The maximum pressure calculated by the Lubrication Approximation was p_{max} =130.15 *MPa* while the simulation gave a maximum pressure of $p_{max.}$=129.5 *MPa* in excellent overall agreement. Again here, the boundary conditions of the flow domain are the same with the Newtonian case described in a previous chapter. The second simulation employed the same geometry as above but the viscosity was described with the power–law model. The pressure distribution with the simulation is shown at Figure 5.15. From a very first glance it can be seen that OpenFOAM over–predicts the maximum pressure of $p_{max.}$=8.51 *MPa*, with respect to the analytical solution derived by Vlachopoulos *et al* [14] in which $p_{max.}$=7.1 *MPa*.

Table 5.2

Calendering geometry from [6]			
R = 125 *mm*	H_o = 0.3 *mm*	W = 450 *mm*	x_f = 4.37 *mm*
H_f = 0.74 *mm*	$V_{roller1}$ = 0.07383 *m/s*	$V_{roller2}$ = 0.07366 *cm/s*	Q =100 *kg/hr*
Viscosity parameters from [6], for power law viscosity model			
m = 46120 *Pa·s*	n = 0.340	ρ_{melt} = 1300 *kg/m*^{3}	

Since this might have been due to the poor domain discretisation, simulations were performed in which the number of cells was increased to 360000 and 760000 and the results are shown at Figure 5.16. Mesh refinement did not affect the behavior of the predicted pressure distribution as it still over–predicts the maximum pressure obtained from the analytical solution from the Lubrication Approximation. Such a behavior of the pressure distribution might occur due to the power–law viscosity model used, which is a two parameter model and subject to limitations when used in a 2D or 3D geometry, as explained earlier. Contrary to the predictions of the power–law model, polymer melts and liquids, at sufficiently low shear rates, exhibit a plateau viscosity which is significantly lower than the viscosity predicted by the power–law model.

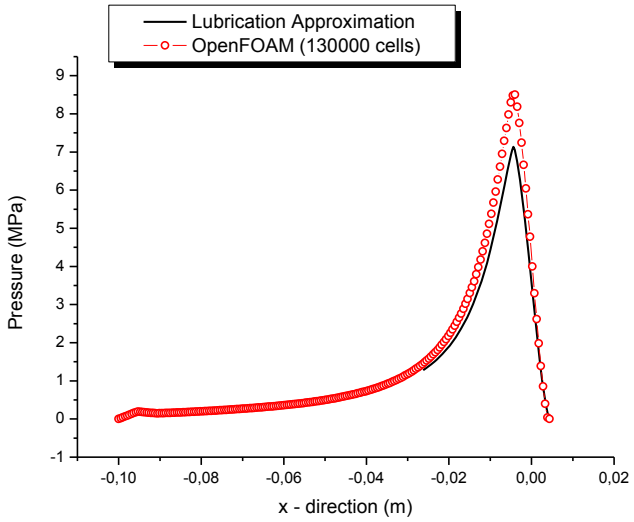

Figure 5.15. Pressure distribution along the x – direction for the computational flow domain filled with 130000 cells and analytical solution with Lubrication Approximation.

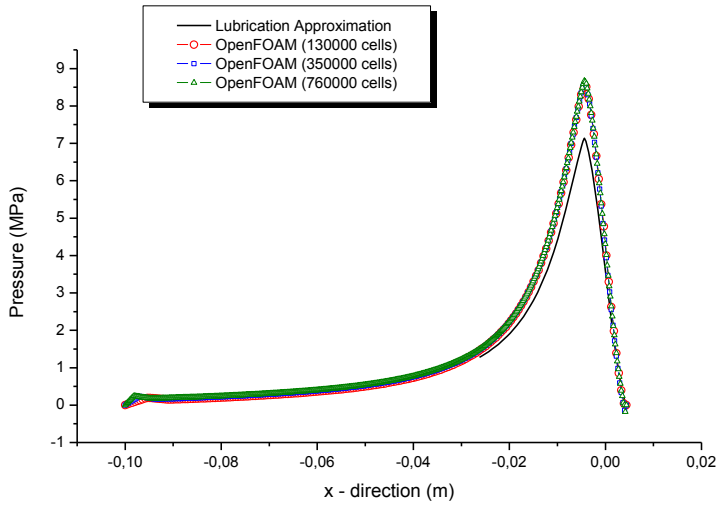

Figure 5.16. Pressure distribution for different number of cells filling the computational flow domain.

This means that at low shear rates they behave as Newtonian fluids. As the shear rate increases, in most polymeric fluids, the viscosity drops (this behavior is often called *shear thinning*), and on double–logarithmic coordinates one often observes nearly straight line behavior at high shear rates. Such a behavior is shown as an example in Figure 5.17 for HDPE. At the same figure it can be concluded that at very low shear rates (i.e. $\dot{\gamma} < 1\ s^{-1}$) the power–law model severely overestimates the viscosity (when $\dot{\gamma} \to 0$

the viscosity tends to infinity ($\eta \to \infty$)). For that reason, the Power – Law model may give erroneous results if used in a flow domain where regions of very low shear rate exist. If someone is to use the power–law model he needs to truncate the viscosity at the very low shear rates region to capture the Newtonian behavior of the material. Obviously, there is no advantage in choosing the simple power–law model whenever finite elements, finite volumes or finite differences are involved and for that reason it should be avoided.

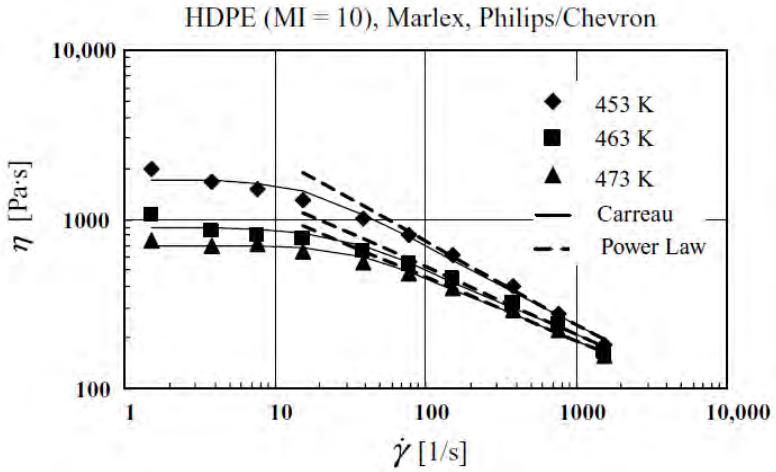

Figure 5.17. Viscosity versus shear rate for High Density PolyEthylene (HDPE) at different temperatures. The points are measured values, the solid lines represent the fit with the Carreau model and the dashed ones with the Power – Law model [2].

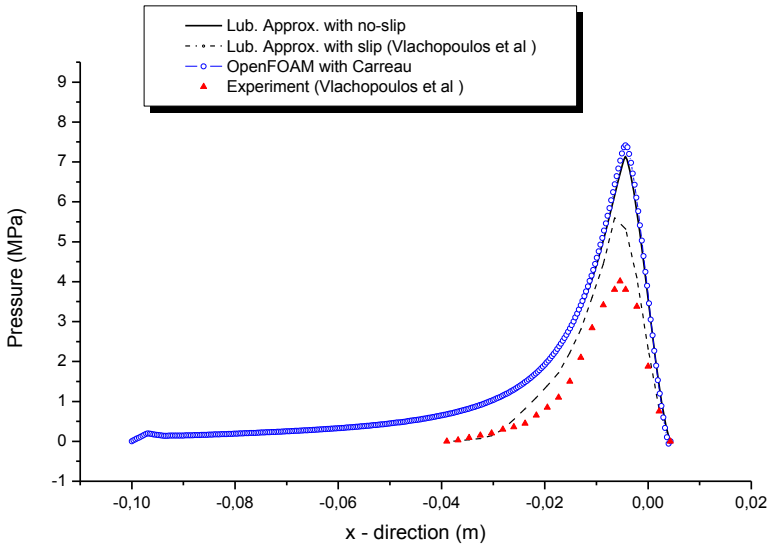

Figure 5.18. Pressure distribution along the centerline with the Carreau viscosity model. Results obtained with OpenFOAM, Lubrication Approximation with no – slip, Lubrication Approximation with slip [14] and experimental measured values [14].

To predict correctly the pressure distribution between the calenders the Carreau viscosity model is employed which is a four parameter model and can predict the viscosity at low shear rates as it can be seen from Figure 5.17. Vlachopoulos and Hrymak [14] in their work do not report any measured viscosity versus shear rate plots nor where the viscosity truncation for the power–law model was carried–out. In the present study it is approximated that the truncation of the viscosity was at 46120 $Pa{\cdot}s$, which means that below 1 s^{-1} of shear rate, the fluid behaves as Newtonian. Thus, in order to employ the Carreau model we approximate that $\eta_0=m_{power\text{-}law}=46120\ Pa{\cdot}s$, for the power–law index $n=0.34$ and $\lambda=1.25\ s$. With such an approximation the Carreau model can fit very well the power–law at the high shear rate region near the nip region. The pressure distribution in the machine direction (centerline) with the Carreau viscosity model is shown at Figure 5.17. The maximum pressure reported by the Lubrication Approximation is 7.1 MPa and the maximum pressure OpenFOAM calculates is 7.4 MPa which is in general in good agreement. The maximum pressure reported by the experiment is 4.02 *MPa*. However, the value of 4.02 *MPa* is measured by a pressure transducer which was located 80 *mm* from the center of the calenders as Vlachopoulos *et al* report and this is a reason why such a deviation exists. Moreover, there was no report in their work for the experimental pressure distribution for the central region along the centerline. The other reason is that the present study has not taken into account any slip phenomena which may take place at the surface of the calenders. The slip velocity at the surfaces of the calenders can be measured. If slip at the calenders is inserted in the Lubrication Approximation then the maximum pressure drops to the value of 5.60 *MPa* as Vlachopoulos *et al* [14] report in their work. However, in the present study slip phenomena where not taken into account.

The numerical experiments carried out for the Newtonian fluid showed excellent agreement with the analytical solution from which the detachment point was calculated and accepted as a sufficient initial guess. However, on an effort to validate the numerical and the experimental work by Vlachopoulos *et al.* [14], our results exhibited a small deviation from the predicted and the experimental values. This was probably because Vlachopoulos *et al.* [14] do not report where the viscosity truncation was done or any measured viscosity versus shear rate curves. Since, the power–law viscosity model

exhibits a peculiarity at very low shear rates, the Carreau viscosity model was the next rational choice, but not the only as someone could use the Cross viscosity model. Provided that we had available viscosity versus shear rate data, the results could be refined and correctly predict the pressure distribution.

Chapter 6

3D Effects in Calendering

Introduction

The problem of rolling of sheets, such as metals and ceramic pastes is an important problem and has been studied extensively using elastic–plastic simulation methods to study two- and three- dimensional flows [37–45]. An interesting approach to study spreading phenomena has been carried out by Matsumiya and Flemmings [46], using the Lubrication Approximation Theory for the production of a metal alloy strip from its molten state. These authors described the rheological behavior of the alloy as a power–law fluid and assumed that the pressure did not vary in the machine direction and the only present velocity is the one along the cross–machine direction for the region between the rollers. Thus the pressure varies only in the cross–machine direction giving a quasi–parabolic pressure profile. Their results are shown at Figure 6.1. Moreover, Sezek *et al.* [47] in their work studied cold and hot metal plate rolling based on a three–dimensional mathematical model considering lateral spread of the plate. They showed that by increasing the thickness reduction of the plate the rolling force increases but decreases with the process temperature. Three dimensional effects in the calendering of thermoplastics have been studied by Unkrüer for the first time in his doctoral thesis [13]. He carried out experiments using a calender having two rolls of 80 mm diameter and 1600 mm length calendering PVC and PS. His conclusions were that (*i*) the calendered sheet spreads and (*ii*) vortices are formed in and near the melt bank as shown

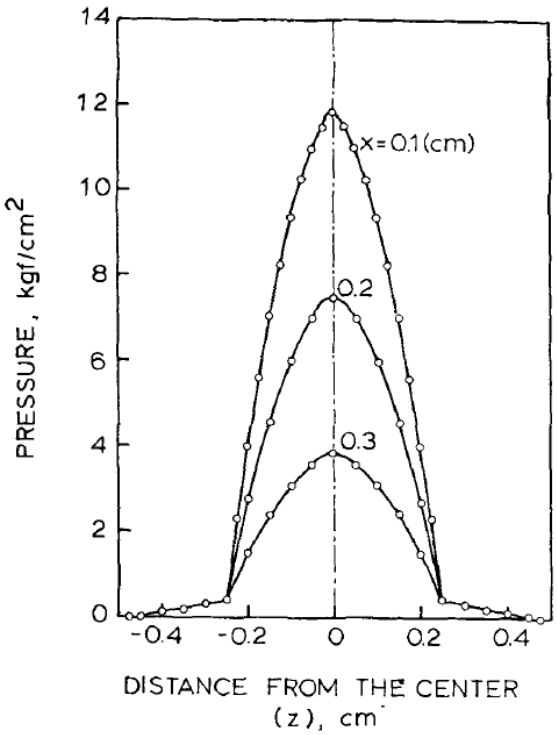

Figure 6.1. Pressure distribution in the cross–machine direction as calculated by Matsumiya and Flemmings [46].

schematically in Figure 6.2. Also, it was observed that in the melt bank the material conveys to the sides through a spiral motion as also shown at Figure 6.2. He also observed, as shown in Figure 6.3, that the pressure drops to zero in the cross–machine direction with the distance from the middle section (centerline) thus resulting in a quasi–parabolic pressure profile as shown at Figure 6.4.

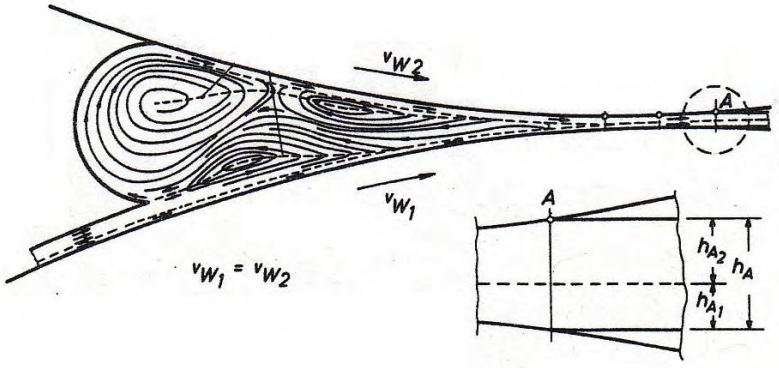

Figure 6.2. Schematic diagram of the vortices in the calendering process as observed by Unkrüer [13]. V_{w1} and V_{w2} are the velocities of the bottom and top roller respectively, A is the point of detachment and h_A is the final sheet thickness.

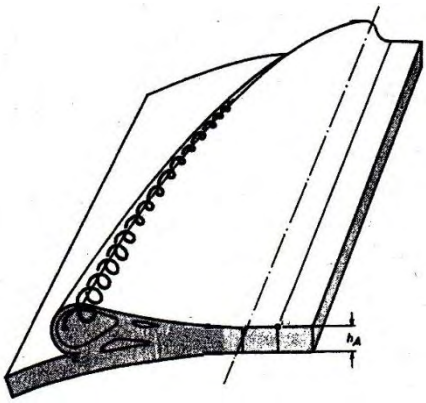

Figure 6.3. Spiral transport of the material, in the melt bank, from the middle region to the sides as observed by Unkrüer [13].

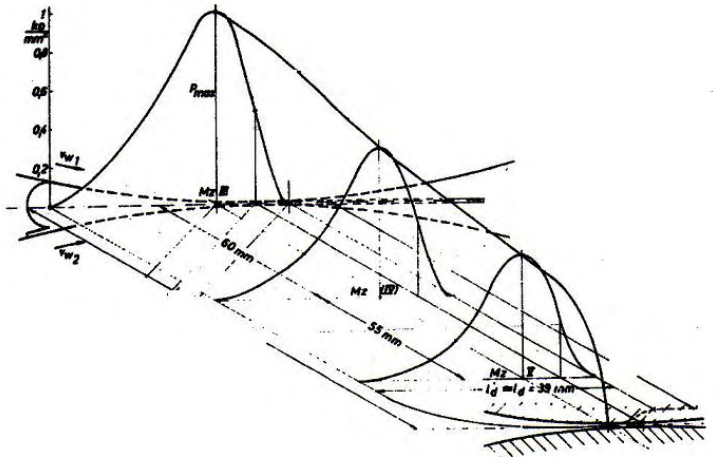

Figure 6.4. Pressure distribution at various cylinder axial positions and in the cross – machine direction near the nip region for rigid PVC as observed by Unkrüer [13]. The roll spread is 50 mm/s for both rolls, roll temperature 185^{o}C, minimum gap of 0.6 mm, roll diameter 300 mm and width 500 mm.

This is how Tadmor and Gogos describe Unkrüer's observations: "The melt accumulates in the center zone of the nip area and simultaneously undergoes flow into the nip and sideways. The drag–induced flow leads to pressure buildup, which inevitably produces pressure gradients in the machine and cross–machine directions". The only known attempt of a 3D simulation of the calendering process was carried out by Luther and Mewes [21]. These authors however did not report any simulation of spreading or the existence of a third vortex (two vortices are predicted by the 2D analysis as explained earlier) or the existence of a quasi–parabolic pressure profile in the direction of the calenders axes (cross–machine direction). Thus, their main result is the spiral motion in

the cross – machine direction as shown at Figure 6.5 which was observed experimentally before by Unkrüer [13].

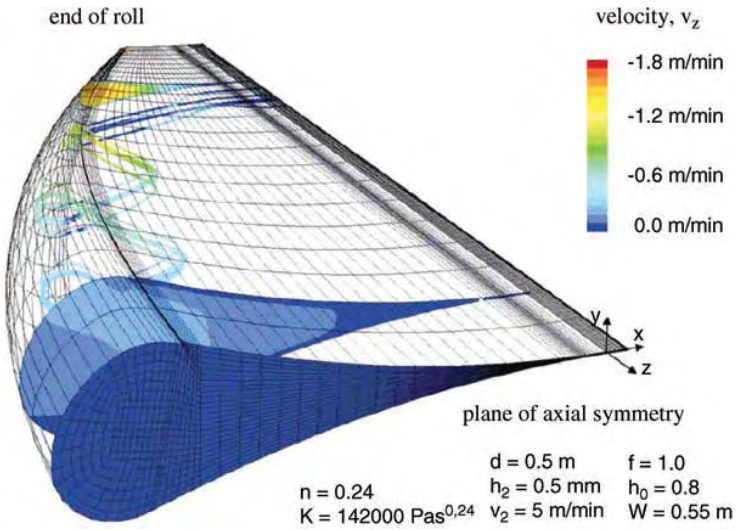

Figure 6.5. Three dimensional simulation results for the calendering of a power – law fluid. In the figure it is shown the computational flow domain along with the spiral motion occurring in the melt bank in the z – direction [21].

Moreover, Levine *et al.* [48] took into account the flow in the cross–machine direction to predict the spreading of a power–law fluid utilizing the simplifications of the Lubrication Approximation. They proposed a two dimensional model to describe the flow field which seems to be similar to the Hele–Shaw approximation model for laterally spreading flows. In the results pressure contours were calculated in the cross machine direction, with the pressure being maximum in the central region of the sheet, but no quasi parabolic pressure profiles were presented. It was also predicted that the sheet spreads more when the nip region between the calenders decreases. However, in his study, there is no reference of the work by Matsumiya and Flemmings [46].

In the present work a different approach is followed using fully 3D Navier–Stokes equations. The spreading of liquids can be found in some publications by Scriven *et al*. [49,50] and by Li *et al.* [51]. From a general point of view, surface tension, is an important property of fluids and in simple words, is the force that keeps the fluid's molecules together. Also, the viscosity of polymer melts is roughly a million times bigger

than the viscosity of a fluid like water ($\mu_{\text{polymers}}=10^3–10^5$ $Pa{\cdot}s$ for polymer melts at usual processing conditions, $\mu_{\text{water}}=10^{-3}$ $Pa{\cdot}s$). However, the surface tension of polymers is about 1/3 of the surface tension of water (e.g. γ_{HMWPE} =29.4 mJ/m^{-2}, γ_{PMMA} =31.7 mJ/m^{-2}, γ_{water}=72.75 mJ/m^{-2}) and for that reason, in polymer melts, surface tension effects are rather small as compared to the viscous effects. In the real process of calendering, as the viscous polymer melt passes through the calenders, it is squeezed. Simultaneously, and very close to the nip region, it spreads in the cross–machine direction to a finite width. Therefore, from a physical point of view, the macromolecular chains in polymer melts are hold together (i.e. the material does not spread infinitely) due to a property that primarily describes solid materials, which is called elasticity. Polymers exhibit a dual behavior, partly as liquids (viscous) and partly as solids (elastic) as described by Ferry [52]. In the case of calendering, the partially elastic nature of the molten polymer does not allow it to spread infinitely. The Navier–Stokes equations do not employ any terms to account for the elastic nature of the material since they describe the flow of liquids. For that reason, the solution of these equations cannot predict how much the polymer will spread in the cross–machine direction. However, if it assumed that the polymer melt fully behaves as a fluid with a very high viscosity and neglect its elastic nature, the applicability of the Navier–Stokes equations is valid. Then, the spreading of the molten material is not calculated from the equations themselves but it is guessed before the solution.

In the following section we describe the flow between the rollers with a purely viscous model (Newtonian and GNF model) so that to investigate the behavior of the flow at the machine and the cross–machine direction. The spreading is determined approximately based on an initial educated guess as it will be explained further on the present study. This assumption is done for the construction of the computational flow domain. A few simulations, as it will be explained, can improve the initial guess of the geometry for the flow domain. The choice of the boundary conditions for pressure and velocity as well as approximate flow domain geometries will be discussed in the following section with a number of simulations for a Newtonian fluid and further on for a Generalized Newtonian Fluid employing the Carreau viscosity model.

6.1 Numerical Results for a Newtonian Fluid

6.1.1 Geometry of Computational Flow Domain and Boundary Conditions

As a first simulation it was chosen, for the geometry of the grid, the experimental dimensions measured by Vlachopoulos and Hrymak [14]. The grid is shown at Figure 6.6 and at Figure 6.7 from another perspective. It was approximated that, for the present case, the geometry variation (width of sheet) from the entrance to the exit is approximated to increase linearly from the entrance to the exit, simulating the spreading of the sheet which occurs during calendering. As described in a previous chapter the roll radius is R=125.00 *mm*, the half gap at the nip region (x=0) is H_o=0.30 *mm*, the final sheet thickness is $2H_f$ =0.74 *mm*, the point of detachment which was derived from the Lubrication Approximation is x_f =4.37 *mm*, the width of the sheet at the entry is $W_{en.}$=225.00 *mm*, the width of the sheet at the very exit is $W_{ex.}$=370.00 *mm*, the velocity of the top roller is V_{top} = 0.07366 *m/s* and for the bottom roller V_{bottom} = 0.07383 *m/s*. For the point of attachment it was approximated, based also on the experimental data of Vlachopoulos and Hrymak, that it is nine times larger than the point of detachment so it was placed at x_i = -37.31 *mm* (the half–thickness of the sheet at x_i is H_i = 6.00 *mm*).

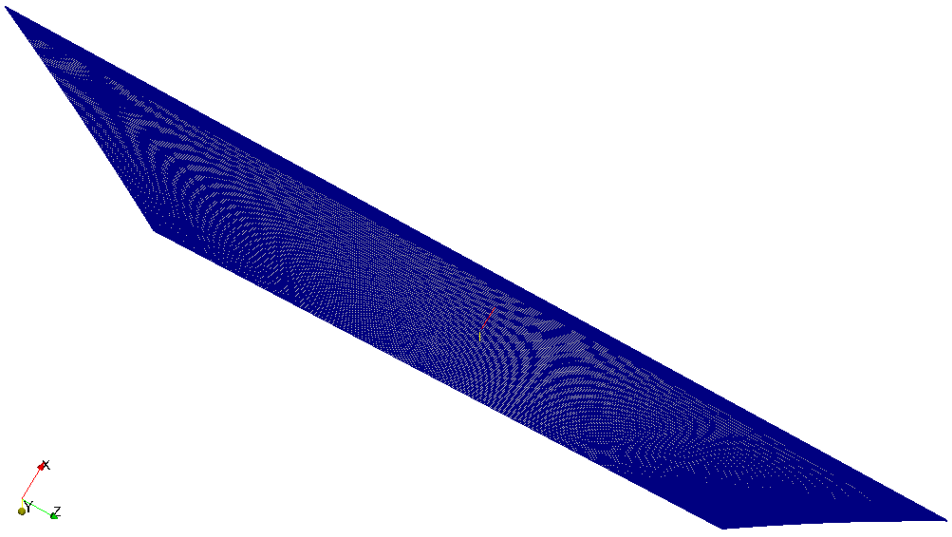

Figure 6.6. Top view of the computational domain for the spreading of the sheet.

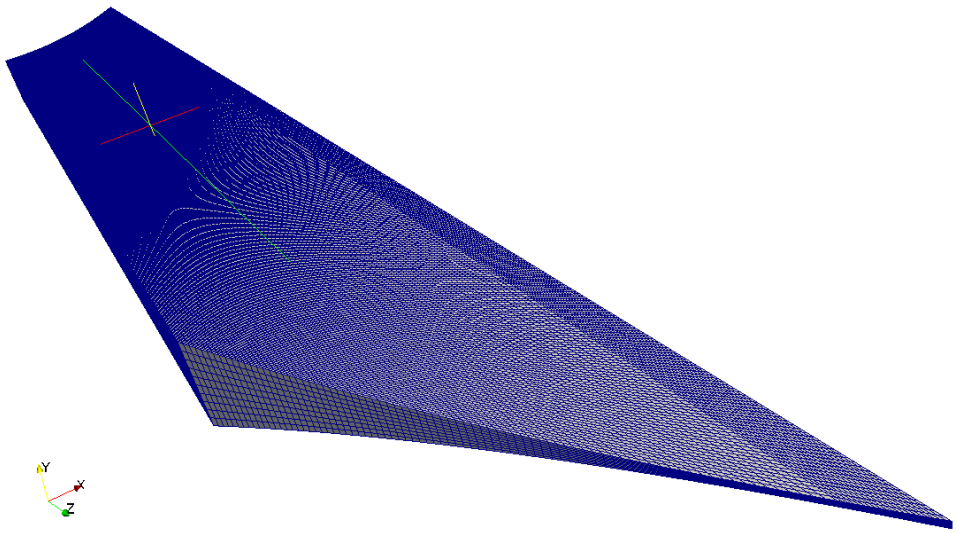

Figure 6.7. Inclined–top view of the computational domain for the spreading of the sheet.

It is also assumed that the feeding of the material, is done from a single screw extruder which is located far behind the calenders. Between the extruder and the calenders it is assumed that a rectangular channel (i.e. a flat die) exists, which is attached directly to the calenders. The width of the channel is $W_{en.}$ and the gap is $2H_i$. By this, it is assumed that the material is confined before it enters to the region between the calenders. A rough sketch of the above is shown at Figure 6.8. A similar calendering process is carried out by Michelis [53] for the production of polymeric strips a few centimeters wide. In the present case the simulation is performed for a Newtonian fluid with a relatively low viscosity, that is μ=1000 $Pa{\cdot}s$ and with ρ=1000 kg/m^3.

One of the most important steps for the simulation, after the construction of the computational flow domain, is to decide the nature of the boundary conditions from a physical point of view. The notation of each boundary can be found in Figure 6.9. In reality, the side boundaries of the domain, where the spreading of the sheet occurs, are free surfaces. A rational approximation that can be done is to accept that these boundaries are in contact with the atmosphere, thus, the pressure can be set equal to zero. A similar boundary condition for side boundaries for the pressure is followed by Luther *et al* [21] and by Levine *et al*. [47].

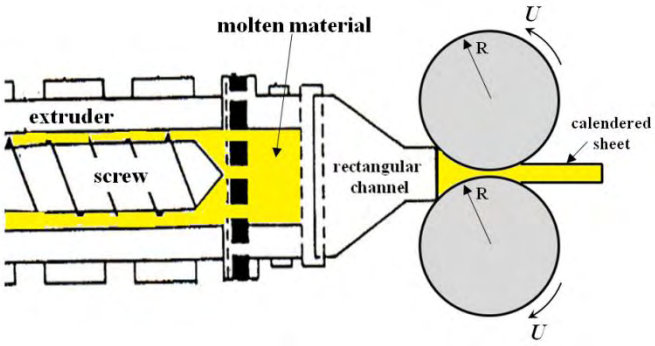

Figure 6.8. Schematic representation of the process employed. The molten material is directly fed from the extruder to the calenders through the rectangular channel. *R* is the radii of the calenders and *U* the velocity.

Moreover, it is also assumed that along the side boundaries, the fluid can slip. For that reason the sides are approximated as surfaces with *perfect slip*. As stated by Weller [28, 29] the *slip* boundary condition for the velocity implies that the normal component has a fixed value and equal to zero (no cross flow takes place) and that the tangential components have zero gradients. Mathematically this is formulated as

$$\mathbf{U}_n = 0 \qquad \text{and} \qquad \frac{\partial \mathbf{U}_t}{\partial \mathbf{n}} = 0 \tag{6.1}$$

Concerning the entrance, as in the two dimensional Newtonian case, the boundary condition for the velocity is the fixed value of the flow rate. For the pressure boundary condition it was decided to set the pressure gradient equal to zero. Mathematically, this can expressed as

$$\frac{\partial p}{\partial \mathbf{n}} = 0 \tag{6.2}$$

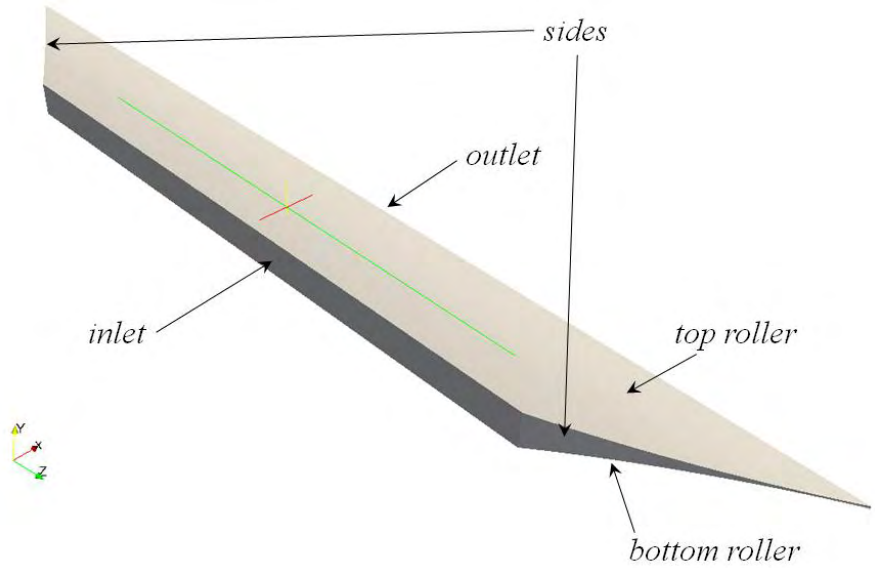

Figure 6.9. Notation of the boundaries on the computation flow domain.

Below, the reader can find summarized the above boundary conditions along with the ones for the rest of the boundaries of Figure 6.9.

- *Top and bottom calenders*
  - Pressure: Normal gradient of pressure is zero, $\frac{\partial p}{\partial \mathbf{n}} = 0$
  - Velocity: tangential velocity $\mathbf{U}_{t,rol.} = V$, normal velocity $\mathbf{U}_{n,rol.} = 0$

- *Sides*
  - Pressure: Fixed value, $p = 0$
  - Velocity: $\mathbf{U}_n = 0$ and $\frac{\partial \mathbf{U}_t}{\partial \mathbf{n}} = 0$ ($\mathbf{U}_n$ is the normal component and $\mathbf{U}_t$ the tangential component)

- *Outlet*
  - Pressure: Fixed value, $p = 0$
  - Velocity: Normal gradient of velocity is zero, $\frac{\partial \mathbf{U}}{\partial \mathbf{n}} = 0$

- *Inlet*
  - Pressure: Normal gradient of pressure is zero, $\frac{\partial p}{\partial \mathbf{n}} = 0$
  - Velocity: Known flow rate $Q = \rho \left| \mathbf{U}_{t,rol.} \right| W_{en.} \left(2H_i \right)$

where $2H_i$ is the distance between the rollers at the inlet.

6.1.2 Results and Discussion

The pressure field of the simulation as obtained with OpenFOAM is shown at Figure 6.10. From a very first glance it can be seen that, at both side boundaries and near the exit, the pressure exhibits negative values. This may be a result of the imposed boundary conditions, combined with the geometry of the computational flow domain. These regions, although they exhibit extremely negative values of pressure, with respect to the maximum positive pressure developed, they are contained only in a small volume of the computational flow domain something which is obvious from Figure 6.10. These regions appear to occur near the exit boundary and adjacent to the two side boundaries. The regions appear to be symmetric with respect to the centerline.

In the real calendering process, the sheet does not spread linearly from the entrance to the exit. Such a claim holds valid, as in Unkrüer's work [13] it is reported that in the narrow region of the nip (minimum distance between the calenders), drag flow caused by the movement of the calenders is predominant as compared to the flow in the cross – machine direction, thus, it can be concluded most of the sheet spreading occurs *before* the material reaches the nip region.

The pressure profiles at different locations are shown at Figure 6.11 and at Figure 6.12 plotted in a three–dimensional form. The pressure profile in the machine direction appears to have the usual bell–shape behavior with the maximum pressure to be approximately 3.17 *MPa*. It can also be seen that near the entrance the pressure exhibits a build–up (short pressure plateau) of approximately 0.76 *MPa* as shown at Figure 6.11.

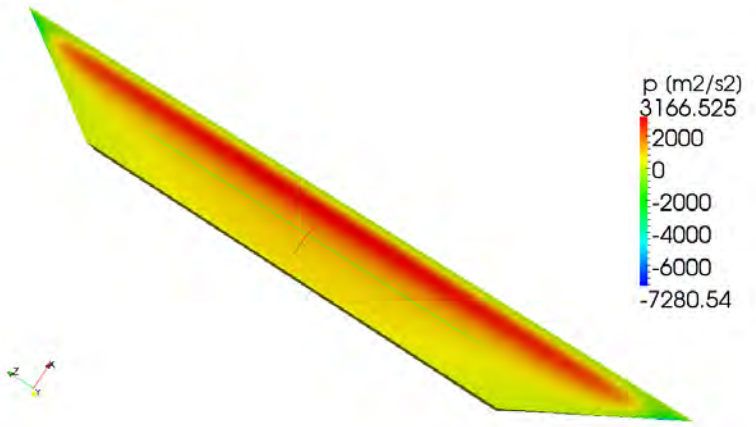

Figure 6.10. Calculated pressure profile for the linear geometry variation (width of sheet).

This is the result of the applied boundary condition of the pressure at the specific boundary. Such a behavior is rational since it was assumed that the material is fed from a rectangular die fitting directly to the calenders. The presence of the calenders and the rectangular die, at the entrance, creates a resistance at the flow thus creating a pressure build–up and this is exhibited by the plateau of the pressure curve, along the centerline and near the entrance. After the built–up the pressure increases to a maximum value due to the rotational movement of the calenders, and then drops to zero at the exit, as dictated by the boundary condition on that boundary. Moreover, at Figure 6.11 the maximum pressure is located at $x=-x_f$ =-4.37 *mm*, thus, validating once again the strength of the Lubrication Approximation (as discussed in Chapter 2).

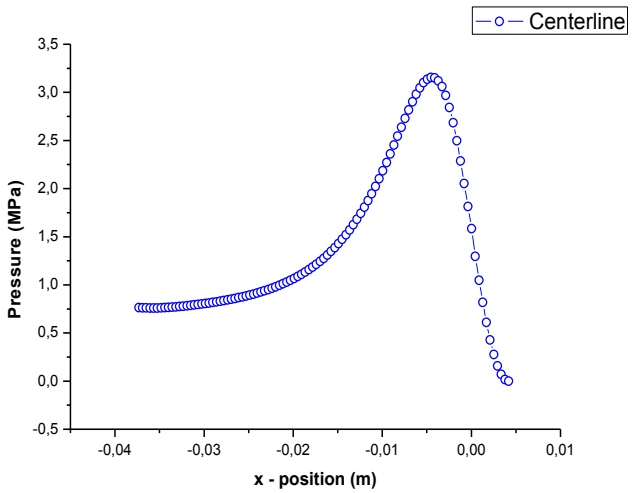

Figure 6.11. Pressure distribution along the centerline located at the middle section of the computational flow domain.

At Figure 6.12 the pressure distribution in the cross machine direction at different locations is shown. The locations at which the pressure distribution was calculated in the cross–machine direction were at x=0, x=-x_f, x=-2x_f and x=-3x_f. The shape of the curve is quasi–parabolic with a maximum at the middle section of the calenders ($W_{en.}$/2=112.50 mm). As we move at the two sides, the pressure starts to level–off, becomes zero, then takes negative values and finally increases to obtain again zero value. Pressure distribution in the cross–machine direction for the position of x=0 (minimum distance between the rollers), appears to have a more flatten profile than at other locations. This effect is due to the rotational movement of the calenders, implying that the pressure gradient does not change much for a large portion of the calenders, thus the predominant flow is the one in the machine direction induced by the rotational movement. This validates the claim presented previously that most of the material spreading occurs before it reaches the nip region. However, there are many values of negative pressure at the sides close to the nip region till the exit. On the other hand, pressure profiles which are near the entrance exhibit a more quasi – parabolic profile and the values of the pressure are all positive or negative but very close to zero.

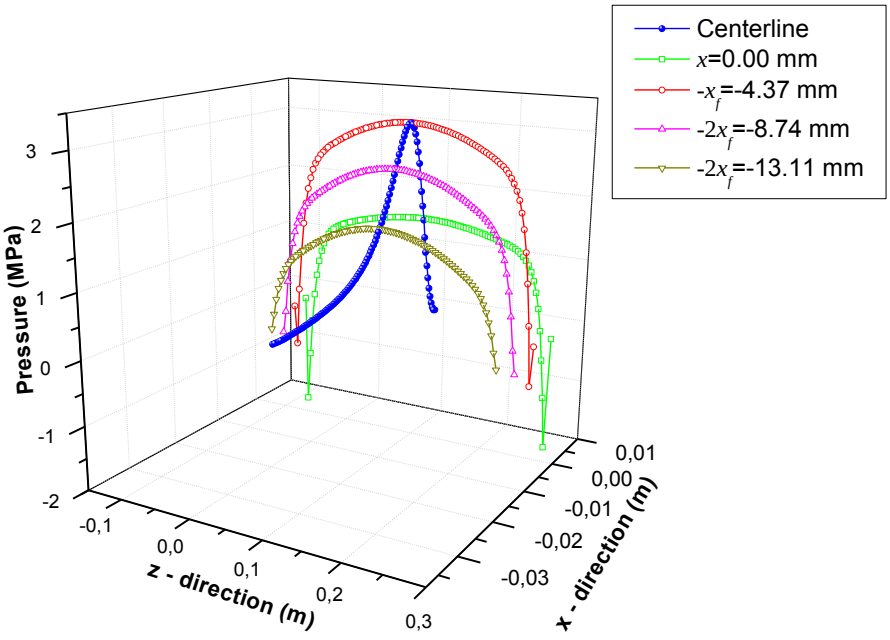

Figure 6.12. Pressure distribution along the x and z direction at different distances for the case of linear width variation.

The pressure distribution in the cross–machine direction, at the nip region (x=0), exhibits a quasi–parabolic profile which is in qualitative agreement with the results of the pressure distribution along the axis of the calenders measured by Unkrüer as shown at Figure 6.13 (The interest lies in the curve that belongs to h_o = 0.25 *mm* since that half–gap is very close to the one of the present study (i.e. h_o = 0.30 *mm*)). The shape of the curves in Unkrüer's study is affected by the distance between the calenders and the presence of the melt bank whose shape also alters in a certain amount the curves. However, in the study presented it was assumed that near the entrance there is no melt bank, the presence of which occurs in the experiment [11-13], which might affect the results. Even though it was adopted that no melt bank was developed near the entrance the results showed a remarkable qualitative agreement with Unkrüer's experimental work.

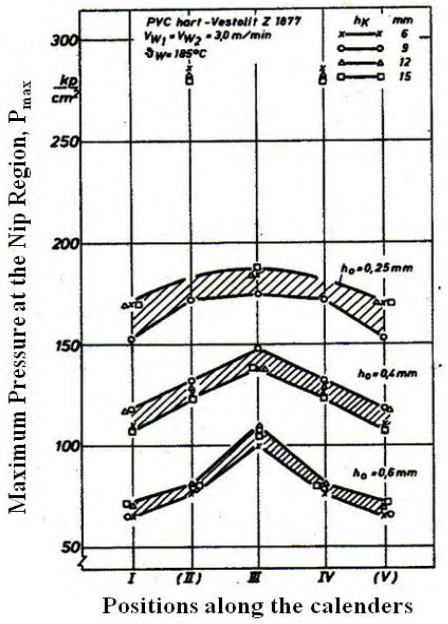

Figure 6.13. Pressure distribution in the cross – machine direction for different minimum gaps (h_o) between the calenders as measured by Unkrüer [13]. h_k is the height of the melt bank and V_{w1}, V_{w2} are the velocity of the calenders.

From the same results, and since the objective of the thesis is to obtain the pressure profile in the cross–machine direction, the imposed boundary conditions seemed to be efficient to describe numerically the calendering process and produce some very interesting and novel findings for the first time, using the fully three–dimensional

Navier–Stokes equations. However, on the effort to predict also a possible shape for the sheet spreading from the entrance to the exit of the flow domain, we need to take into account the presence of the negative pressure regions. If we set as a point of reference those regions and how to eliminate or to minimize them, it can be concluded that, although the boundary conditions describe sufficiently the process, the linear spreading seems to be only good as a starting guess. For those reasons, the next step is to construct a flow domain at which the sheet spreads linear to a finite width from the entrance to some point behind the nip region. From that point till the exit it is assumed that the spreading is terminated and the width of the sheet remains the same until the exit.

Closer examination of the results of Figures 6.10 and 6.12, reveals that in the machine direction, the negative pressure regions exist approximately between $-2x_f$ and x_f. An educated guess to eliminate those regions would be to construct the flow domain in way that the width of the sheet geometry varies linearly from x_i to $-2x_f$ and from $-2x_f$ until the exit there is no any geometrical variation of the sheet's width. The new flow domain is shown at Figure 6.14.

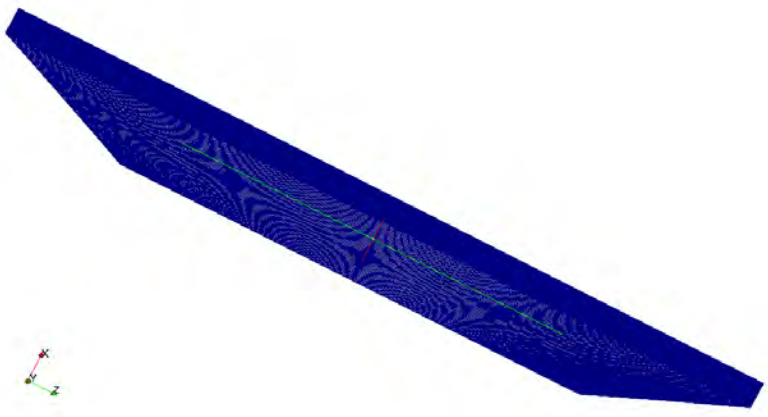

Figure 6.14. Computational flow domain with the spreading of the sheet terminated before the exit.

For the computational flow domain constructed above the calculate pressure field as obtained by the simulation is shown at Figure 6.15. The boundary conditions were assumed to be the same as in the previous simulation. It is clear from the figure, that the

negative pressure regions which appeared in the previous simulation are minimized if compared to Figure 6.10. These regions appear to be near the two side boundaries and at the exit. The approximated shape of the sheet caused a decrease in the negative pressures (absolute value) which means that the assumption of linear width variation to a specific position before the nip region seems reasonable to be assumed. Of course this is only an approximation that we assume and this is why regions with negative pressure still exist. At the side boundaries, where the width of the sheet remains constant, no negative pressure regions were observed. The negative values lie near the exit boundary and the two sides where the width varies linearly.

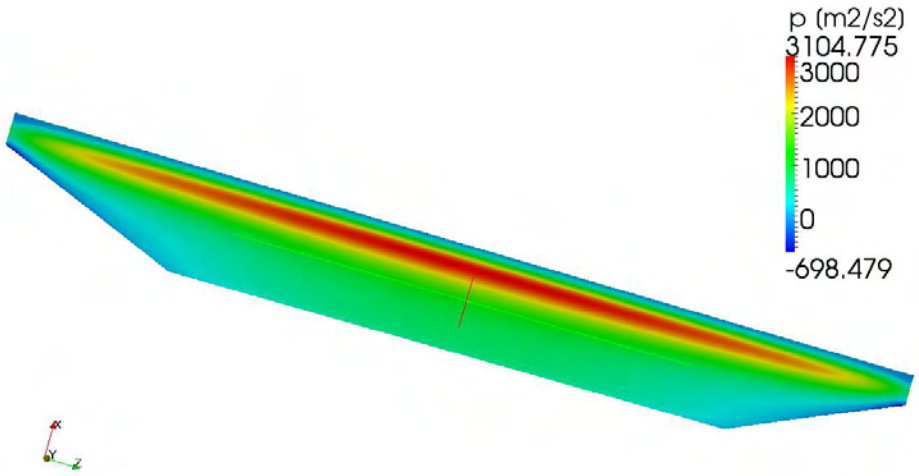

Figure 6.15. Calculated pressure field for the case where the spreading terminates near the nip region.

The pressure distribution along different directions and positions is shown at Figure 6.16. It can be seen that the plotted curves exhibit almost the same behavior as in the previous analysis if compared to Figure 6.12 (the pressure distribution curves are plotted at exactly the same positions as in the previous simulation concerning the linear spreading from the entrance to the exit of the computational flow domain). Although the shape of the flow domain was approximated with a different manner than the previous numerical experiment, the pressure curves preserve their quasi – parabolic behavior (the maximum pressure seems to be unchanged with regard to the previous simulation), implying that the assumed boundary conditions describe satisfactory the problem. Even

closer comparison of Figure 6.12 and Figure 6.16, it can be seen at the latter figure, that the pressure distribution in the cross–machine direction exhibits a "more" quasi–parabolic shape, which means that the pressure gradients exhibit a larger change as we move from the central region to the sides. Near the exit boundary, the pressure distribution in the cross–machine direction appears to have a more flatten profile as it was reported in the previous three–dimensional numerical experiment. Moreover, near the sides the pressure values for the positions of $-x_f$ =-4.37 *mm* and x=0 are all positive. For the position of $-2x_f$ =-8.74 mm, some of the calculated pressure values hold negative numbers, the absolute values of which are smaller if compared to the maximum pressure developed by the simulation.

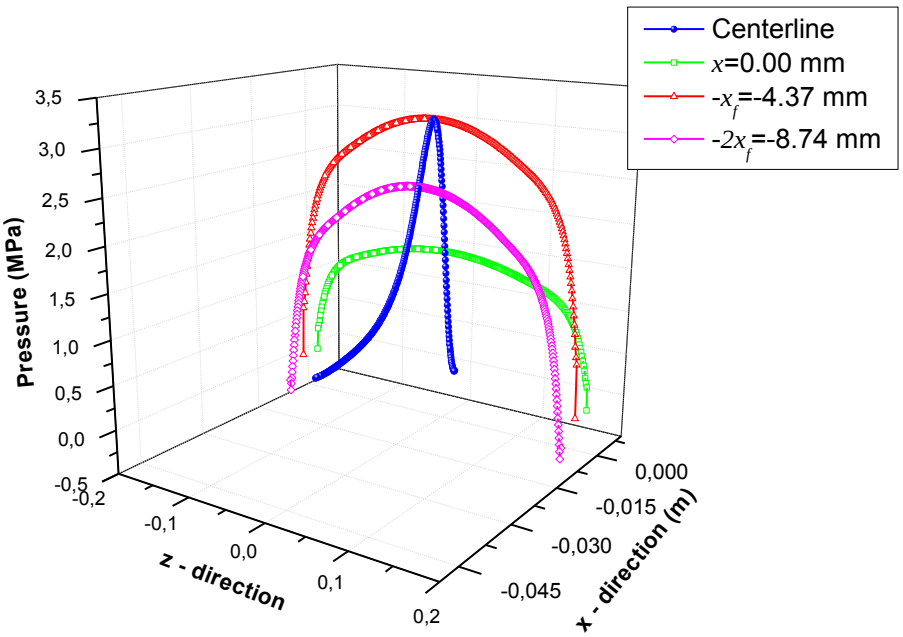

Figure 6.16. Pressure distribution along the x and z direction at different distances for the case of linear width variation from the entrance to $-2x_f$.

The streamlines as calculated by the simulation are showed at Figure 6.17. The behavior of the streamlines shows the spiral transport of the material from the entrance to the two sides and to the exit of the computational flow domain. The material conveys from the entrance of the domain to the two side boundaries and simultaneously progresses to the exit of the domain. This spiraling motion is in qualitative agreement with the numerical results by Luther and Mewes [21] and with the experimental results

observed by Unkrüer [13]. The only difference is that in the present analysis there is not any melt bank. In a sense, it can be assumed that the spiraling motion in the present simulation belongs to a hypothetical melt bank. Moreover, the spiraling is caused due to the imposed boundary conditions for pressure and velocity at the side boundaries which force the material to flow, except the machine direction, also in the cross–machine direction implying the existence of velocity component u_z. The velocity field for u_z is presented at Figure 6.18 for different cross–sectional areas normal to the z–axis and at Figure 6.19 for a cross–section normal to the y–axis. It can be seen that u_z is greater in two regions, which appear to be symmetrical, located between the entrance and the two sides. The negative values are due to the minus z–axis. In the middle region, u_z is approximately zero which means that the sheet does not spread close to that region and this is why at Figure 6.17 the spiraling effect of the streamlines is less intense.

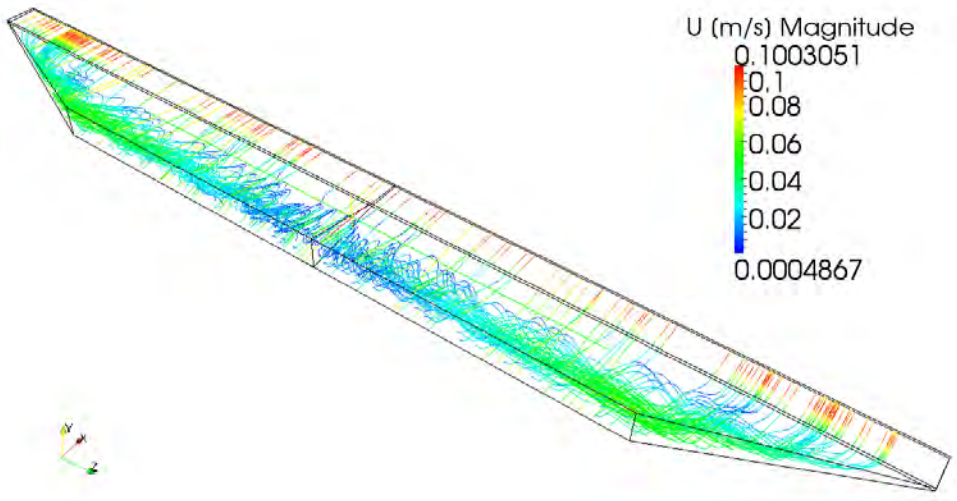

Figure 6.17. Calculated streamlines for the case where the spreading terminates at -2x_f. The legend refers to the magnitude of the velocity.

Another result of the imposed boundary conditions is that some of the streamlines in Figure 6.17, terminate at the side boundaries while some others start from the entrance, they progress tangentially to the side boundaries and they finally terminate at the exit boundary of the domain. This implies that from the two sides there is outflow. The outflow seems to be greater from the wider area of the side boundaries. From the narrower area of the same boundary, the outflow is much less. This seems to be rational

since in the nip region the flow in the x–direction is predominant and the flow in the z–direction is less intense. Of course, the assumptions done previously are only an initial reasonable approximation to describe the flow between the calenders. The negativity of the pressure seems to be more prone to the shape of the computational domain rather than the imposed boundary conditions. However, these approximations can be refined, especially for the geometry of the side boundaries and a parabolic or a quasi–parabolic shape could probably eliminate or minimize the negative pressure regions. The present study gave only a sufficient insight on how to construct an appropriate computational flow domain to describe the hydrodynamics of the flow as well as the prediction of pressure distribution in the cross–machine direction.

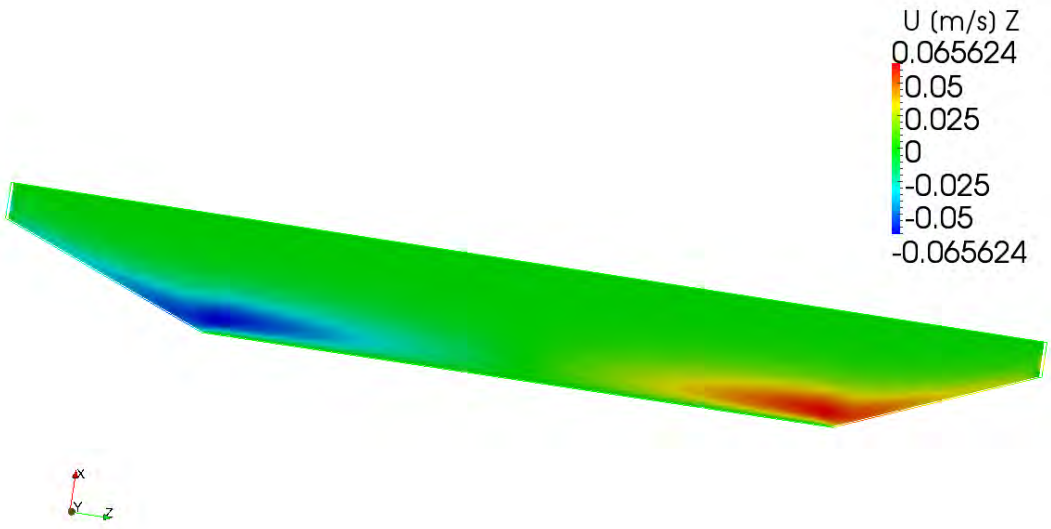

Figure 6.18. Top view of the velocity field for the velocity component u_z for a cross – sectional area which is normal to the y–axis.

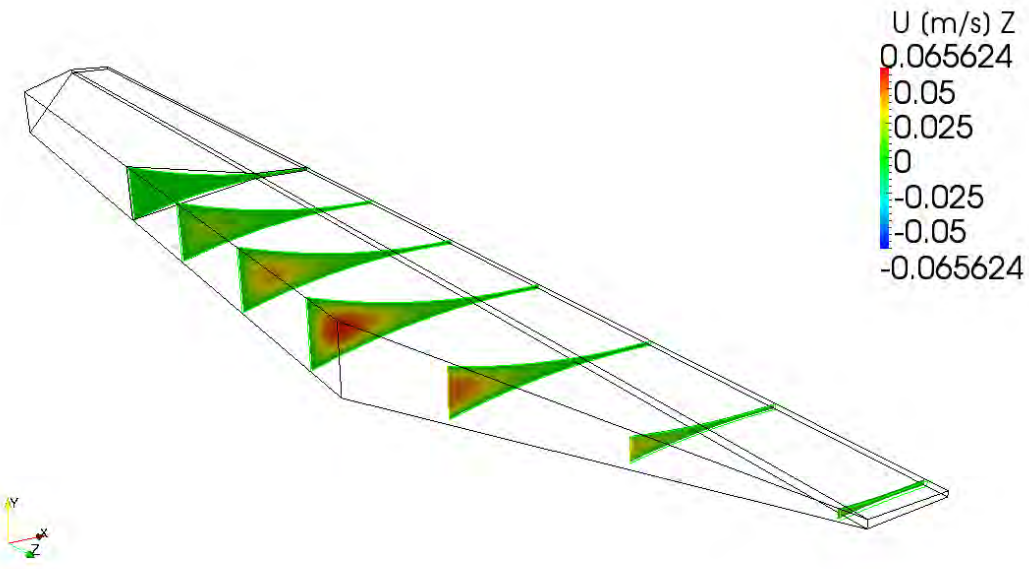

Figure 6.19. Inclined view of the velocity field for the velocity component u_z for different cross – sectional areas normal to the z–axis.

In the present simulation, as well as in the previous one, the shape of the computational domain was determined based on a set of boundary conditions and a pre–determined spreading which was improved after a single simulation. The spreading of the sheet is the result of the imposed boundary conditions combined with the shape of the computational flow domain. The observed velocity in the cross–machine direction, u_z, is the result of the pre–determined geometry. Thus, the fluid must spread so that to fill the expanding geometry.

6.2Numerical Results with Carreau Viscosity Model

6.2.1 Geometry, Spreading of the Sheet and Boundary Conditions

In the previous simulations, the Newtonian viscosity model gave very satisfactory results, most of which are in qualitative agreement with past theoretical and experimental studies [13,21,44]. In the present section the Carreau viscosity model is employed for the simulations. The geometry for the computational domain is obtained from the study by Vlachopoulos and Hrymak [14] and the spreading is considered to be the one presented in the final three dimensional simulation above, for the Newtonian fluid where the

spreading terminates at $-2x_f$. Thus, the computational domain is the one shown at Figure 6.14. The parameters for the Carreau viscosity model are the ones presented in the two–dimensional study in Chapter 5. For the boundary conditions, it seemed rational to impose the ones used in the three–dimensional Newtonian analysis of the previous section. The way the material is fed in the inlet is the one described in the previous analysis, illustrated at Figure 6.8. The aim of the present simulation is not to validate the work done by Vlachopoulos *et al.* [14]. From their work we only obtained geometrical and rheological parameters. Our formulation is in the scope of presenting qualitative results for the pressure distribution in the cross – machine direction, spiraling movement of the material near the entrance (with no presence of melt bank) and approximate spreading of the sheet. Results by Unkrüer [13] and Luther et al. [21] provide the necessary information for such a qualitative comparison.

6.2.2 Results and Discussion

The pressure distribution for the computational domain is presented at Figure 6.20. The computed field appears to have similar pressure behavior with the previous three–dimensional simulations for the Newtonian fluid with the pressure now being higher. It can be seen, in the same figure, the presence of negative regions as in the previous simulations. Such a result was anticipated due to the approximations of the boundary conditions and the shape of the computational flow domain, as it was discussed in the previous section. For that reason, we can conclude that the viscosity model used each time does not affect the presence of negative regions in the flow domain.

The pressure distribution in the machine and cross – machine direction at different positions is presented in Figure 6.21. The maximum pressure is reported to be approximately p_{max}=9.1 *MPa*. The pressure distribution along the centerline has the well known bell–shape shape. Near the entrance there is a relatively large pressure built–up which is caused by the obstruction of the flow, as it was assumed that exactly before the calenders there is attached a rectangular die from where the polymer melt is fed. In the nip region (x=0) the pressure profile in the cross – machine direction is more flatten if compared to the rest of the curves of Figure 6.21, implying that the dominant flow is

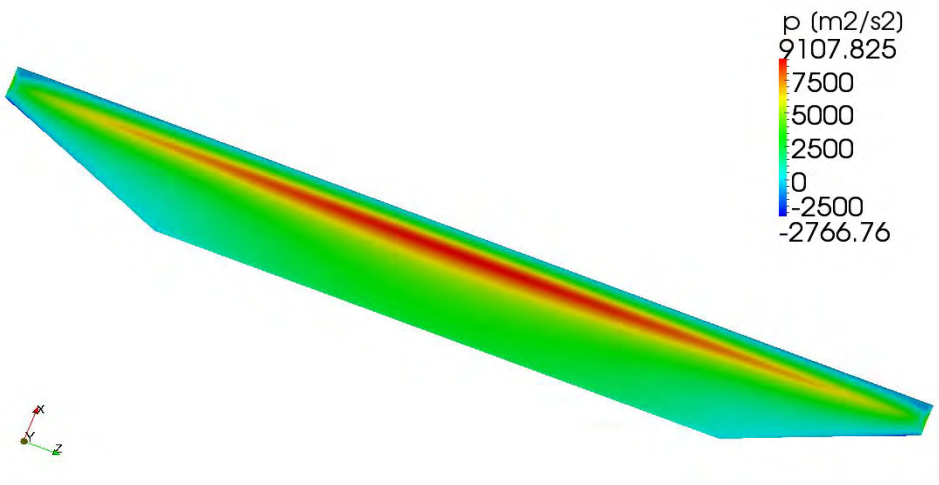

Figure 6.20. Calculated pressure field with the Carreau viscosity model.

due to the rotational movement of the calenders, thus the spreading of the sheet is small as the pressure gradient does not change much in the z–direction. At x=-x_f and for x<-x_f the pressure profiles exhibit a “more” quasi – parabolic profile, and the rapid change of the pressure gradients imply the rapid spreading of the sheet. However, as we move near

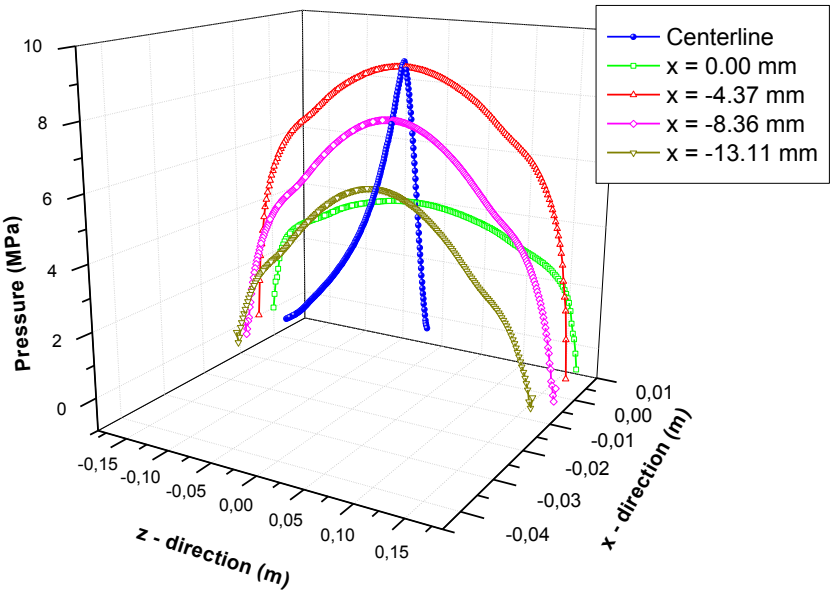

Figure 6.21. Pressure distribution in the machine and cross – machine direction at different positions with the Carreau viscosity model.

the entrance, there are some negative pressure values near the two side boundaries. For the present simulation it was accepted that the obtained absolute value of the negative pressure is the maximum that can be numerically obtained with the present set of boundary conditions and the computational domain geometry. The total elimination of the negative regions would require a more thorough examination of the shape of the computational domain, especially for the two side boundaries, and also decide where the spreading of the sheet terminates. Of course, the lack of melt bank near the entrance of the computational domain affects somehow the results but since the present analysis is on the scope of a qualitative study, if someone compares Unkrüer's results shown at Figure 6.13 a lot of qualitative similarities can be found with the present work. So far, there are not any reports in the open literature for quasi – parabolic pressure profile in the cross–machine direction using the fully 3D Navier – Stokes equations along with a Generalized Newtonian Fluid model. Thus, we are the first to obtain qualitative results by the use of the above approximations. A more elegant approach, could employ the determination of the shape of the side boundaries on the basis that the width of the sheet does not vary linearly, but in a parabolic or quasi – parabolic manner. The exact shape for the spreading can be determined through several iterations concerning the shape of the side boundaries in a way that the streamlines near the boundary do not cross it but lie tangentially to it.

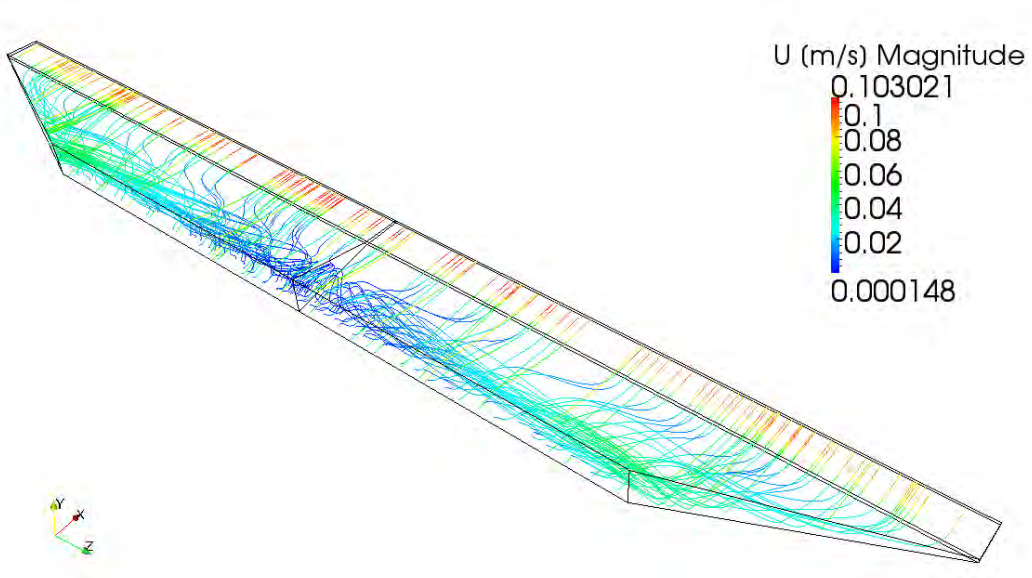

Figure 6.22. Calculated streamlines for a polymer melt obeying the Carreau viscosity model.

Furthermore, at Figure 6.22, the calculated streamlines of the flow domain is presented. In the central region the spiraling effect is less intense and it becomes greater as the material progresses to the two side boundaries. Some of the streamlines end directly to the side boundaries and some others end at the exit boundary. For those streamlines that terminate at the side boundaries, the material can outflow from the greater area of the sides, whereas from the smaller area the outflow, if any, is small due to the fact that the rotational movement of the calenders create a dominant drag flow in the nip region that forces the material to flow in the machine direction rather than spread.

For those reasons, the side boundaries are not treated, strictly speaking, as free surfaces. The partly elastic nature polymer melts hold, prevents them to spread infinitely on such a process. Thus, the present boundary conditions seemed rational to be assumed. In a matter of speaking it is approximated that the liquid–elastic material is treated, with a purely viscous model like most fluids. To account for the finite spreading we assumed a set of boundary conditions that seemed to be rational from a physical point of view, and imposed them on the spirit of preventing the material to spread infinitely. Of course, outflow from the side boundaries is not a desirable parameter. However, the results showed qualitative agreement with theoretical and experimental past studies but there is always room for improvement.

As a final result of the present numerical experiment, we show the velocity profiles of $U_{mag.}$, u_x and u_z at different locations of the computational domain, along the y–direction. The different locations are represented schematically at Figure 6.23.

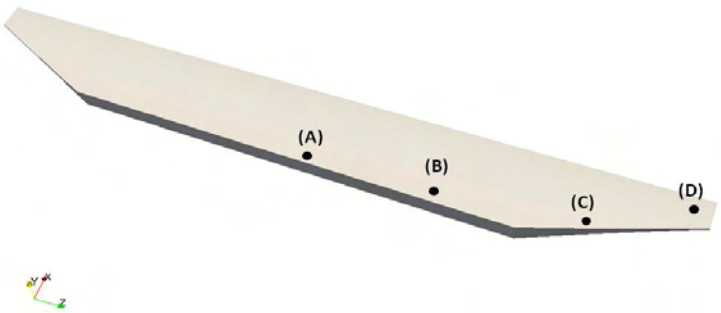

Figure 6.23. Schematic representation of the locations for the velocity profiles along the y–axis.

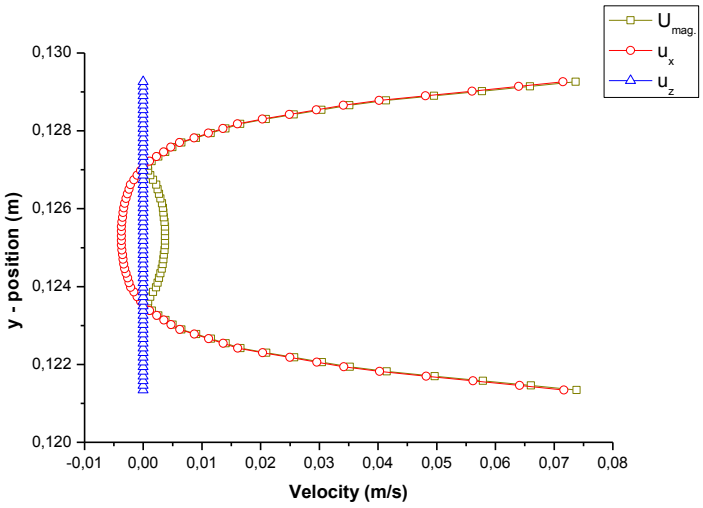

Figure 6.24. Velocity profiles for location (A).

At Figure 6.24, u_x is higher near the calenders and decreases in the mid–plane (the plane normal to y–axis) taking negative values. The negative values are due to the recirculation patterns predicted by the numerical experiment and imply backflow in the machine direction. This is also why $U_{mag.}$ profile has the shape shown at the figure which means that the material's velocity increases to a certain value near the centerline but it moves backwards. Simultaneously, at that location (A), u_z holds zero (or very small) velocity values which means that the material does not flow in the cross machine direction, thus does not spread. If we move from that location a few centimeters, either to the one side or the other, u_z holds higher values which means the sheet is assumed to spread thus resulting in the spiral motion discussed above and showed at Figure 6.22 which appears to be weak close to location (A) and intense as the material progresses to the sides.

In Figure 6.25, at position (B), the velocity component u_z, appears to have a quasi–parabolic pressure profile similar to the well known parabolic velocity profile for a pressure driven flow between two flat plates. The velocity magnitude $U_{mag.}$ profile in the same figure, seems to have higher values than in location (A) and this is due to the contribution of the velocity in the z–direction as the fluid is conveyed downstream and in

the machine direction. This velocity, as discussed extensively in previous sections, is the result of the applied boundary conditions at the side boundaries of the flow domain and

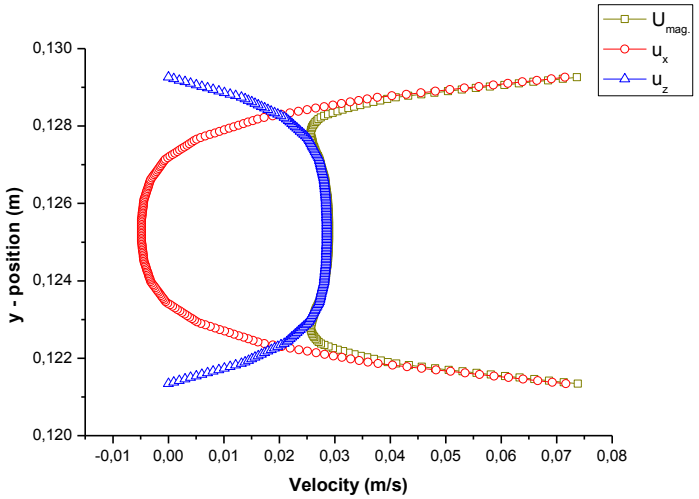

Figure 6.25. Velocity profiles for location (B).

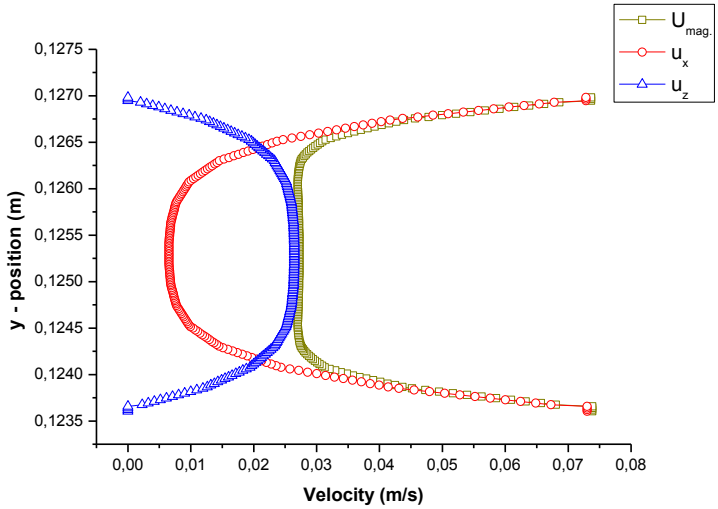

Figure 6.26. Velocity profiles for location (C).

the shape of the geometry. Similar behaviors seems to have the velocity profiles at location (C) as shown in Figure 6.26. The velocity component u_z, appears to have a quasi–parabolic profile which means that the material is conveyed in the z–direction. From the u_x velocity profile, it can be seen that there are no negative values which means that there is not any back flow, thus the circulatory patterns do not occur at that location.

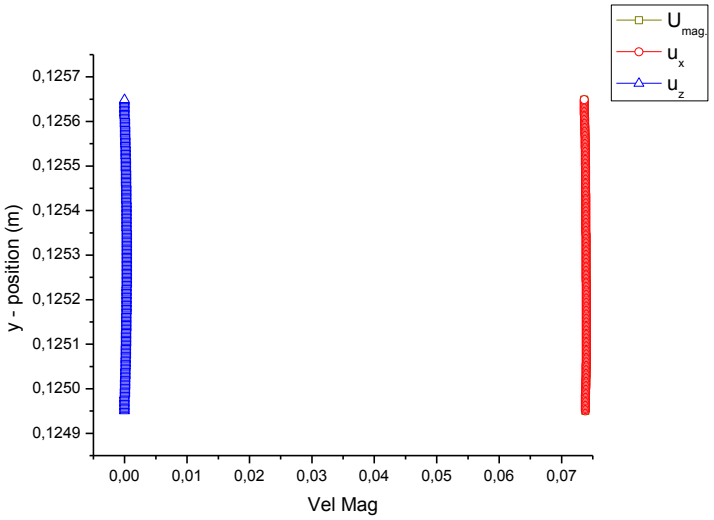

Figure 6.27. Velocity profiles for location (D).

The velocity magnitude $U_{mag.}$ profile shown at the same figure, reveals that the velocity is maximum near the calenders and drops to an approximately constant value near the mid–plane x–z. Near that plane, the velocity is almost the same to the maximum velocity in the z–direction, thus the dominant flow occurs in that direction.

The final plotted velocity profiles are near the exit, at location (D), and are presented at Figure 6.27 with the velocity profile downstream being almost constant ($U_{mag.}$=u_x=0.0783 m/s) and the velocity in the cross – machine direction very low or zero values. This implies, that the sheet at the exit has very close velocity with the velocity of the calenders.

Closure and Future Work

The proposed objectives of the present thesis were to predict the pressure distribution in the cross–machine direction as well as a sufficient geometry with varying width of the calendered sheet by the help of *OpenFOAM*. The study was initiated by validating a previous work on calendering using the Newtonian and the Generalized Newtonian Fluid models. For the Newtonian Fluids the numerical experiments exhibited excellent agreement with the Lubrication Approximation Theory. However, the peculiarity of the power–law model, combined with the lack of measured rheological data, gave erroneous results and for that reason the Carreau viscosity model was utilized giving results with good overall agreement. The study for the three–dimensional flow between the calenders for Generalized Newtonian Fluids, with the assumption that no melt bank occurs, gave results which were in qualitative agreement with past numerical and experimental studies. The results gave some very interesting insight into the quasi–parabolic pressure distribution in the cross–machine direction and the shape of the calendered sheet as it spreads. Thus, the present work is so far the only one that can predict the above, employing the Navier – Stokes equations by means of a Generalized Newtonian Fluid model and making several reasonable approximations throughout the study. Of course, there is always room for improvement.

The inability of the Navier–Stokes equations to predict the partly elastic behavior of the material is a limiting parameter for such a study. However, by making special assumptions the material can be treated as a purely viscous fluid. In future work, special care needs to be taken for the side boundaries. The linear width variation proposed here, is only the one side of the coin. The other side would require an effort to express those

sides with a parabolic or quasi–parabolic shape. This can be performed by a certain number of simulations in the scope of the calculated streamlines do not cross the side boundaries, thus no outflow from these sides should occur. Moreover, another assumption that needs to be taken into account is the presence of melt bank and on what extend its shape affects the results. Finally, another important aspect that someone should embody in the study is the non–isothermal study of the process. This can be done by inserting and solving simultaneously with the Navier–Stokes, the energy equation and also introducing temperature dependence of the viscosity models.

Bibliography

1. Middleman S., *Fundamentals of Polymer Processing*, McGraw–Hill, New York, USA, **1977**
2. Tadmor Z., Gogos C., *Principles of Polymer Processing*, John Wiley & Sons, New Jersey, USA, **2006**.
3. Gujati D.P., Leonov A.I., (Eds), *Modeling and Simulation in Polymers*, Wiley–VCH Verlag GmbH & Co. KGaA, Weinheim, Germany, **2010**.
4. Cogswell F.N., *Melt Rheology*, Woodhead Publishing, Cambridge, **1996**
5. Gaskell R.E., *The Calendering of Plastic Materials*, J. App. Mech.,17, 334–337, **1950**
6. McKelvey J.M., *Polymer Processing*, Wiley, New York, USA, **1962**.
7. Brazinsky I., Cosway H.F., Valle Jr. C.F., Clark R., Jones R., Story V., *A Theoretical Study of Liquid–Film Spread Heights in the Calendering of Newtonian and Power–Law Fluids*, J. App. Polym. Sci., 14, 2771–2784, **1970**
8. Alston W.W., Astill K.N., *An Analysis for the Calendering of Non–Newtonian Fluids*, J. App. Polym. Sci., 17, 3157–3174, **1973**
9. Kiparissides C., Vlachopoulos J., *Finite Element Analysis of Calendering*, Polymer Engineering and Science, 16 (10), 712–719, **1976**
10. Kiparissides C., Vlachopoulos J., *A Study of Viscous Dissipation in the Calendering of Power–Law Fluids*, Pol. Eng. Sc., 18 (3), 210–214, **1978**.
11. Agassant J.F., Espy M., *Theoretical and Experimental Study of the Molten Polymer Flow in the Calender Bank*, Pol. Eng. Sci. 25 (2), 118–121, **1985**.
12. Agassant J.F., *Le Calandrage des Matières Thermoplastiques*, Doctoral Thesis, Paris 6, France, **1980**.
13. Unkrüer, *W., Beitrag zur Ermittlung des Drucksverlaufes und der Fliessvorgange im Walzspalt bei der Kalanderverarbeitung von PVC Hart zu Folien*, PhD Thesis, IKV, TU Aachen, **1970**.
14. Vlachopoulos J., Hrymak A.N., *Calendering Poly(Vinyl Chloride): Theory and Experiments,* Pol. Eng. Sci., 20 (11), 725–731, **1980**.

15. Mitsoulis E., Vlachopoulos J., and Mirza, F.A., *Calendering Analysis Without the Lubrication Approximation*, Polym. Eng. Sci., 25, 6–18, **1985**.
16. Vlachopoulos, J. and Mitsoulis, E., *Fluid Flow and Heat Transfer inCalendering: A Review*, Transport Phenomena in Polymeric Systems–2, vol. VI (eds. M.R. Kamal, R.A. Mashelkar, and A.S.Mujumdar), Advances in Transport Processes, Wiley Eastern, New Delhi, 79–104, **1988**.
17. Sofou S., Mitsoulis E., Calendering of Pseudoplastic and Viscoplastic Sheets of Finite Thickness, Journal of Plastic Film & Sheeting, 20 (3), 185 – 122, **2004**
18. Mitsoulis E., Sofou S., Calendering Pseudoplastic and Viscoplastic Fluids with Slip at the Roll Surface, J. App. Mech., 73 (2), 291–299, **2006**
19. Kovacs J., Mandjarov R., Blisnjuk T., Prehn K., Sussiek M, Muller J, Schulte K., Bauhofer W, *On the Influence of Nanotube Properties, Processing Conditions and Shear Forces on the Electrical Conductivity of Carbon Nanotube Epoxy Composites*, 20,1–6, **2009**.
20. Syehan T., Gojny F., Tanoglu M., *Schulte K., Critical Aspects Related to Processing of Carbon Nanotube/Unsaturated Thermoset Polyester Nanocomposites*, Eur. Polym. J., 43(2), 374–379, **2007**.
21. Luther S., Mewes D., *Three–Dimensional Polymer Flow in the Calender Bank*, Pol. Eng. Sc. 44 (9),1642–1647, **2004**.
22. Patankar, S.V., Spalding D.B., *A Calculation Procedure for Heat, Mass, and Momentum Transfer in Three–Dimensional Parabolic Flows*, Int. J. Heat Mass Transfer, 15, 1787–1806, **1972**.
23. Weller H., *OpenFOAM User Guide*, OpenCFD Limited, www.opencfd.co.uk, **2004**.
24. Jasak H., *Error analysis and estimation for the finite volume method with applications to fluid flows*, PhD Thesis, Imperial College London, **1996**.
25. Versteeg H.K., Malalasekera W., An Introduction to Computational Fluid Dynamics The Finite Volume Method, Longman Scientific & Technical, London, UK, **1995**
26. Hestenes M.R., Stiefel E., Methods of Conjugate Gradients for Solving Linear Systems, J. Res. Natl. Bur. Stand., 49, 409–436, **1952**

27. Breuer M., *Direkte Numerische Simulation und Large–Eddy Simulation turbulenter Strömungen auf Hochleistrungsrechnern*, Habilitationsschrift, Universität Erlangern–Nuerberg, Berichte aus der Stroemungstechnik, Shaker Verlag, Aachen, **2002**.
28. Biswas G., Breuer M., Durst F., Backward–Facing Step Flows for Various Expansion Ratios at Low and Moderate Reynolds Numbers, J. Fluids Eng., 126, 362–374, **2004**.
29. CALENDERCAD software, Polydynamics, Inc., Dundas, Ontario, Canada
30. Weller H., *OpenFOAM Programmer's Guide*, First Edition, OpenCFD Limited, www.opencfd.co.uk, **2004**.
31. Zheng R., Tanner R.I., *A Numerical Analysis of Calendering*, J. Non–Newtonian Fluid Mech., 28, 149–170, **1988**.
32. Mitsoulis E., *Finite Element Analysis of Two–Dimensional Polymer Melt Flows*, PhD Thesis, McMaster University, **1984**.
33. Mitsoulis E., *Numerical Simulation of Calendering Viscoplastic Fluids*, J. Non – Newtonian Fluid Mech., 154, 77–88, **2008**.
34. Silliman W.J., Scriven L.E., *Separating Flow Near a Static Contact Line: Slip at a Wall and Shape of a Free Surface*, J. Comp. Phys., 34, 287–313, **1980**.
35. Jay P., Piau J.M., Kissi N. E., Cizeron J., *The Reduction of Viscous Extrusion Stresses and Extrudate Swell Computation Using Slippery Exit Surfaces*, J. Non–Newtonian Fluid Mech. 79, 599–617, **1998**.
36. Mitsoulis E., *Some Issues Arising in Finding the Detachment Point in Calendering of Plastic Sheets*, J. Plastic Film and Sheeting, 26, 141–165, **2010**.
37. Peck M.C., Rough S.L., Wilson D.I., *Roller Extrusion of a Ceramic Paste*, Ind. Eng. Chem., 44, 4099–4111, **2005**.
38. Kim N, Kobayashi S., *Three dimensional simulation of gap controlled plate rolling by the finite element method*. Int. J. Mach. Tools Manuf., 30, 269–81, **1990**.
39. Hwang S.M., Joun M.S., Kang Y.H., *Finite element analysis of temperatures, metal flow and roll pressure in hot strip rolling*, Trans. ASME, J Ind., 115, 290–98, **1993**.

40. Dvorkin E.N., Goldschmit M.B., Cavaliere M.A., Amenta P.M., Marini O., Stroppiana W., 2D *finite element parametric studies of the flat rolling process*., J. Mater. Process Tech., 99–107, **1997**.
41. Lee J.D., A *large strain elastic–plastic finite element analysis of rolling process*, Comp. Met. App. Mech. Eng., 161, 315–47, **1998**.
42. Komori K., *Rigid-plastic finite element method for analysis of three dimensional rolling that requires small memory capacities*, Int. J. Mech. Sci., 40, 479–91, **1998**.
43. Jiang Z.Y., Tieu A., *A simulation of three-dimensional metal rolling processes by rigid-plastic finite element method,* J. Mater. Process Technol., 112, 144–51, **2001**.
44. Duan X., Sheppart T., *Three dimensional thermal mechanical coupled simulation during hot rolling of aluminium alloy 3033,* Int. J. Mech. Sci., 44, 2155–72, **2002**.
45. Jiang Z.Y., Tieu A.K., Zhang X.M., Lu C., Sun W.H., *Finite element simulation of cold rolling of thin strip*., J. Mater. Process Technol., 140, 542–7, **2003**.
46. Matsumiya T., Flemings M.C., *Modeling of Continuous Strip Production by Rheocasting*, Metallurgical Transactions B, 12B, 17–31, **1981**.
47. Sezek S., Aksakal B., and Can Y., *Analysis of Cold and Hot Plate Rolling Using Dual Stream Functions*, Materials and Design, 29, 584–596, **2008**.
48. Levine L., Corvalan C.M., Campanella O.H., Okos M.R., *A Model Describing the Two–Dimensional Calendering of Finite Width Sheets*, Chem. Eng. Sci., 57, 643–650, **2002**.
49. Teletzke G.F., Davis H.T., Scriven L.E., *How Liquids Spread on Solids*, Chem. Eng. Comm., 55, 41–81, **1987**.
50. Huh C., Scriven L.E., *Hydrodynamic Model of Steady Movement of a Solid/Liquid/Fluid Contact Line*, 35, 1, 85–101, **1971**.
51. Li D., Gu Y., *A model for liquid drop spreading on a solid surface*, Colloids Surfaces A: Physicochem. Eng. Aspects, 142, 243–256, **1998**.
52. Ferry J.D., *Viscoelastic Properties of Polymers*, 3rd Edition, John Wiley & Sons, U.S.A.,
53. Michelis P., IMMG S.A., Personal communication.